



Inferring iron oxides species content in atmospheric mineral dust from DSCOVR EPIC observations

Sujung Go^{1,2}, Alexei Lyapustin², Gregory L. Schuster³, Myungje Choi^{1,2}, Paul Ginoux⁴, Mian Chin², Olga Kalashnikova⁵, Oleg Dubovik⁶, Jhoon Kim^{7,8}, Arlindo da Silva², Brent Holben² and Jeffrey S. Reid⁹

- 5 ¹ University of Maryland Baltimore County, Baltimore, MD, USA
² NASA Goddard Space Flight Center, Greenbelt, MD, USA
³ NASA Langley Research Center, Hampton, VA, USA
⁴ Geophysical Fluid Dynamics Laboratory, Princeton, NJ, United States
⁵ Jet Propulsion Laboratory, California Institute of Technology, Pasadena, CA, USA
10 ⁶ Laboratoire d'Optique Atmosphérique, Université de Lille-1, CNRS, Villeneuve d'Ascq, France
⁷ Yonsei University, Seoul, Korea
⁸ Particulate Matter Research Institute, Samsung Advanced Institute of Technology, Korea
⁹ US Naval Research Laboratory, Monterey, CA, USA

Correspondence to: Sujung Go (sujung.go@nasa.gov)

15 **Abstract.** The iron-oxide content of dust in the atmosphere and most notably its apportionment between hematite (α -Fe₂O₃) and goethite (α -FeOOH) are key determinants in quantifying dust's light absorption, its top of atmosphere UV radiances used for dust monitoring, and ultimately shortwave dust direct radiative effects (DRE). Hematite and goethite column mass concentrations and iron-oxide mass fractions of total dust mass concentration were retrieved from the Deep Space Climate Observatory (DSCOVR) Earth Polychromatic Imaging Camera (EPIC) measurements in the ultraviolet–visible (UV–Vis)
20 channels. The retrievals were performed for dust-identified aerosol plumes using aerosol optical depth (AOD) and spectral imaginary refractive index provided by the Multi-Angle Implementation of Atmospheric Correction (MAIAC) algorithm over six continental regions (North America, North Africa, West Asia, Central Asia, East Asia, and Australia). The dust particles are represented as an internal mixture of non-absorbing host and absorbing hematite and goethite. We use the Maxwell–Garnett effective medium approximation with carefully selected complex refractive indices of hematite and goethite that produce mass
25 fractions of iron oxides species consistent with *in situ* values found in the literature to derive the hematite and goethite volumetric/mass concentrations from MAIAC EPIC products. We compared the retrieved hematite and goethite concentrations with *in situ* dust aerosol mineralogical content measurements, as well as with published data. Our data display variations within the published range of hematite, goethite, and iron-oxide mass fractions for pure mineral dust cases. A specific analysis is presented for 15 sites over the main dust source regions. Sites in the central Sahara, Sahel, and Middle East exhibit a greater
30 temporal variability of iron oxides relative to other sites. Niger site (13.52°N, 2.63°E) is dominated by goethite over Harmattan season with median of ~2 weight percentage (wt.%) of iron-oxide. Saudi Arabia site (27.49°N, 41.98°E) over Middle East also exhibited surge of goethite content with the beginning of Shamal season. The Sahel dust is richer in iron-oxide than Saharan and northern China dust except in Summer. The Bodélé Depression area shows a distinctively lower iron-oxide concentration



(~1 wt.%) throughout the year. Finally, we show that EPIC data allow to constrain the hematite refractive index. Specifically, we select 5 out of 13 different number of hematite refractive indices widely variable in published laboratory studies by constraining the iron-oxide mass ratio to the known measured values. Provided climatology of hematite and goethite mass fractions across main dust regions of the Earth will be useful for dust shortwave DRE studies and climate modeling.

1 Introduction

Aeolian dust, suspended in the troposphere at a rate of 1–4 Pg yr⁻¹, persists for 1–7 days or longer depending on particle size (Boucher et al., 2013). Such dust emissions are caused by saltation in desert regions, seasonal river discharges, and anthropogenic land use (e.g., overgrazing; Ginoux et al., 2012). Airborne dust contributes to the direct radiative effect (DRE) by absorbing or scattering solar and terrestrial radiation in the shortwave (SW, 0.185–4.0 μm) and longwave (LW, 3.33–1,000 μm) spectral regions, respectively (Di Biagio et al., 2020). However, these dust absorption/scattering properties may change substantially during transport with dust chemical composition and size distribution varying over different source regions and with time. Accurate information on the space-time variability of dust spectral absorbing/scattering properties is therefore crucial in estimating direct radiative forcing (Samset et al., 2018).

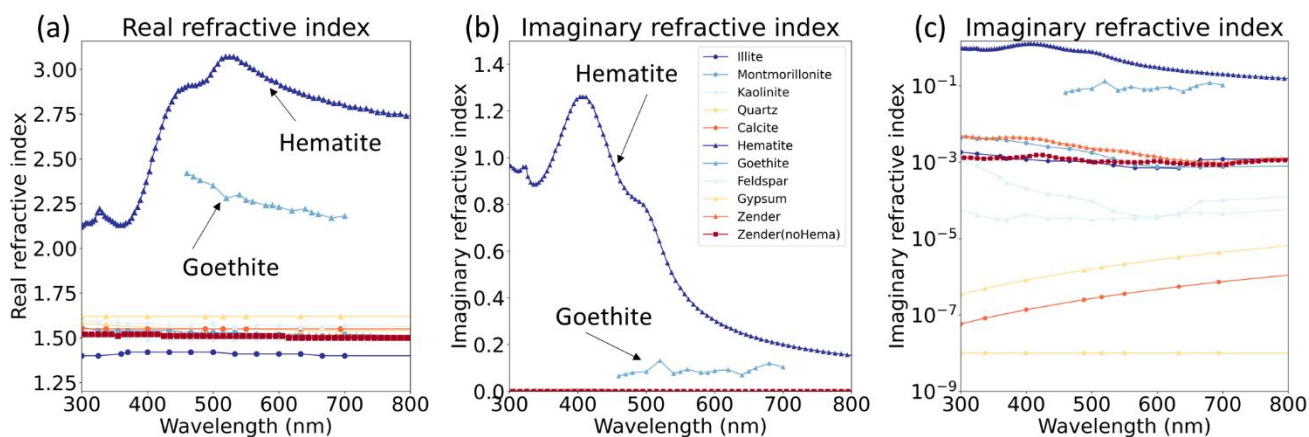
The dust DRE at the top of the atmosphere (TOA) is unresolved in both sign and magnitude. For example, Kok et al. (2017) suggested that the net (SW + LW) dust DRE is cooling at -0.20 W m⁻² with an uncertainty range of -0.48 to +0.20 W m⁻², based on the complex refractive index from Optical Properties of Aerosols and Clouds (OPAC) database (Hess et al., 1998; Volz, 1973). Di Biagio et al. (2020) also suggested cooling at a lower rate of -0.03 W m⁻² with an uncertainty range of -0.29 to +0.23 W m⁻², based on obtained complex refractive indices of different types of mineral dust (Di Biagio et al., 2017; Balkanski et al., 2007). Li et al. (2021) determined a warming effect of +0.04 W m⁻² with an uncertainty range of -0.23 to +0.35 W m⁻², based on CAM5 with a complex refractive index proposed by Scanza et al. (2015). Uncertainties in SW DRE are generally greater than those of LW DRE. The DRE of “pure” mineral dust is determined mainly by its particle size distribution, mineral composition, and particle shape (Sokolik and Toon, 1999; Knippertz and Stuut, 2014) as well as the absolute dust concentration and the height and profile of the dust layer in the atmosphere. Previous studies have pointed out that current climate models use a globally invariant spectral complex refractive index (and therefore spectral single scattering albedo (SSA); Scanza et al., 2015; Samset et al., 2018; Di Biagio et al. 2019), which implicitly assumes the same dust mineralogical composition on a global scale.

A few Earth-system models (ESM’s, i.e., coupled climate models) have adopted regionally and temporally variable spectral refractive index of dust by parameterization with common soil mineralogy components (Scanza et al. 2015; Perlwitz et al. 2015a, b). The rationale for this is that dust aerosols are soil particles suspended in the atmosphere (Scanza et al., 2015). Specifically, in CAM5 (Scanza et al., 2015; Liu et al., 2012), dust aerosol emission mineralogy is transformed from clay-sized [diameters D_p = 0–2 μm] and silt-sized [D_p = 2–50 μm] particles in soil mineralogy to bimodal aeolian dust size distributions



65 (accumulation mode $D_p = 0.1\text{--}1.0\ \mu\text{m}$; coarse mode $D_p = 1\text{--}10\ \mu\text{m}$) by brittle fragmentation theory (Kok, 2011). The dust
aerosol refractive index is then calculated using a volume-weighted mixing rule for all mineral components including water.
Mineral components are internally mixed within each particle mode, and externally mixed between different particle modes
(Liu et al., 2012, 2016). Finally, radiation is simulated by CAM5 for SW and LW spectral regions. The direct radiative forcing
of dust is determined by the difference between the results of two calculations: radiative forcing with all aerosol species, and
70 radiative forcing with all aerosol species except mineral dust. In short, dust radiative forcing is highly dependent on mineral-
specific dust absorption properties in the CAM5 ESM.

Li et al. (2021) recently quantified the importance of soil mineralogical content uncertainty on the dust DRE estimate
using the soil atlases C1999 (Claquin et al., 1999) and J2014 (Journet et al., 2014), with the addition of goethite to C1999.
They concluded that the iron-oxide fraction in dust represents 97% of the uncertainty in their estimated total dust DRE (-0.23
75 to $+0.35\ \text{W m}^{-2}$) using CAM5 only, and 85% across multiple climate models. They also highlighted the importance of
speciation of iron oxides into hematite and goethite to better estimate the SW dust DRE, without which the model would
underestimate dust warming by 56% because the absorption magnitudes of hematite and goethite are up to an order of
magnitude different at ultraviolet (UV) and visible (Vis) wavelengths (Fig. 1).



80 **Figure 1: Complex refractive index based on soil mineralogy at 300–800 nm (Scanza et al., 2015). Shown are the real refractive index (a) and the imaginary refractive index in linear (b) and log (c) scales. Goethite refractive index is from Bedidi and Cervelle (1993).**

Hematite ($\alpha\text{-Fe}_2\text{O}_3$) and goethite ($\alpha\text{-FeOOH}$), both in the Fe(III) oxidation state, are the major iron-oxide species (also referred together as “free iron” or “iron oxides”) in mineral dust (Lafon et al., 2004), and exert major control on the absorption magnitude of pure dust for SW radiation (e.g., Sokolik and Toon, 1999; Arimoto et al., 2002; Lafon et al., 2006; Formenti et al., 2014a), as can be inferred from their complex imaginary refractive index (Fig. 1). The imaginary index magnitudes of both
85 hematite and goethite ($10^{-1}\text{--}10^0$) are more than 100 times those of other soil mineral components ($10^{-8}\text{--}10^{-3}$) at wavelengths of $<1\ \mu\text{m}$, which means that hematite and goethite dominate absorption while other minerals can be considered non-absorbing.



Hematite imaginary index (0.2 at 700 nm to 0.8 at 460 nm) is generally about three times higher than that of goethite (~0.1) (Bedidi and Cervelle, 1993) in the red–near infrared (NIR), the discrepancy further increasing towards blue–UV. At 350–450 nm, the imaginary index of hematite peaks at 1.0–1.2, whereas it changes little for goethite remaining at ~0.1. This significant difference in spectral absorption between hematite and goethite facilitates their separate retrievals.

Despite its high radiative impact on SW dust DRE, the relative proportion of iron oxides in the total dust mass is very small (up to 6.5 weight percentage-wt.%; Schuster et al., 2016). Iron oxides also control the color of soil (Torrent et al., 1983). A reddish color indicates hematite (hues of 5YR and 10R) and yellowish-brown colors indicate goethite (hues of 7.5YR and 2.5Y) in soils, with the range of hues depending on the concentration, crystal size, and degree of cementation (Schwertmann, 1971; 1993). Hematite and goethite generally occur together in both soil and in the atmosphere, and they are internally mixed with other mineral particles, whereas most other dust minerals are externally mixed (Formenti et al., 2014a). Their formation in soil is influenced by climate change, with cooler and more humid conditions favoring goethite formation owing to changes in the organic-matter regime of the soil (Schwertmann, 1971).

The GRASP-components algorithm (Li et al., 2019) uses the Maxwell–Garnett effective medium approximation to provide aerosol speciation from the Polarization and Anisotropy of Reflectances for Atmospheric science coupled with Observations from a Lidar (PARASOL) developed for the POLarization and Directionality of the Earth’s Reflectances (POLDER) program. Several future satellite missions such as Multi-Angle Imager for Aerosols (MAIA) (Diner et al., 2018) and Earth Surface Mineral Dust Source Investigation (EMIT) (Green et al., 2020) will be providing aerosol composition or mineralogical information. The Earth Polychromatic Imaging Camera (EPIC) instrument has been operational since 2015, while POLDER/PARASOL was decommissioned in December 2013.

Several studies used regional or global AEROSOL ROBOTIC NETWORK (AERONET) inversion products (Arola et al., 2011; Koven and Fung, 2006; Schuster et al., 2005, 2016) or ground-based data (Li et al., 2013, 2015; Wang et al., 2013) to retrieve aerosol components.

This study retrieves hematite and goethite volume fractions and mass concentrations in atmospheric mineral dust from the EPIC UV–Vis (340, 388, 443, 680 nm) data, based upon the above physical characteristics of hematite and goethite. We began with Multi-Angle Implementation of Atmospheric Correction (MAIAC) retrieved spectral aerosol absorption information, i.e., the imaginary index at 680 nm (k_o) and spectral absorption exponent (b) (Lyapustin et al., 2021), currently optimized for “pure” smoke or dust.

The methodology is based on the Maxwell–Garnett effective-medium approximation and follows the work of Schuster et al. (2016). Assuming atmospheric aerosols are inhomogeneous particles with different complex dielectric functions, the Maxwell–Garnett approximation can be used to calculate average dielectric functions because of the interactions of electromagnetic waves between inhomogeneous particles (Bohren and Huffman, 1983). The theory considers randomly inhomogeneous mixtures comprised of two inclusions embedded in a homogeneous matrix (Bohren and Huffman, 1983). With



120 the host considered a homogeneous matrix with inclusions of hematite and goethite, we undertook component retrievals from dust-identified aerosol plumes with the MAIAC EPIC algorithm over six continental regions following Schuster et al. (2016) with some modifications. One issue with hematite is that its spectral refractive indices obtained in laboratory studies are varying widely (Schuster et al., 2016; Zhang et al., 2015). We examine how the volume fractions of hematite and goethite change with the hematite refractive index in Sections 2.3 and 4.

125 The remainder of this paper is organized as follows. Section 2 describes the input data and methodology; Section 3 presents the results of selected case studies (Sec. 3.1), a comparison with *in situ* soil measurements (Sec. 3.2), and a summary of regional-seasonal climatology (Sec. 3.3); Section 4 presents elimination analysis of different hematite refractive index models consistent with EPIC UV–Vis measurements and *in situ* iron-oxide mass ratio. The results of this work are summarized in the concluding Section 5.

130 2 Data and methodology

2.1 v2 MAIAC EPIC Algorithm

The EPIC aboard the DSCOVR satellite has been providing observations of the sunlit side of Earth from the first Lagrangian point (L1) since 2015. EPIC provides hourly measurements of the sunlit part of the Earth as it rotates from sunrise to sunset. Such a capability has not previously been available from any other spacecraft or Earth-observing platform. Following
135 the Moderate Resolution Imaging Spectroradiometer (MODIS) MAIAC algorithm (Lyapustin et al., 2018), the MAIAC EPIC algorithm over land provides cloud detection, retrieval of aerosol optical depth (AOD) with regionally specified background aerosol models, and atmospheric correction. Recently, we expanded the MAIAC EPIC algorithm to include simultaneous retrieval of AOD and spectral imaginary refractive index for the detected absorbing aerosols, e.g. biomass burning smoke and mineral dust (Lyapustin et al., 2021). Spectral absorption in MAIAC is represented by a power-law expression,

$$140 \quad k_{\lambda} = k_0(\lambda/\lambda_0)^{-b}, \text{ where } \lambda_0 = 680 \text{ nm} \quad (1)$$

where k is an imaginary refractive index. The real refractive index and the size distribution for smoke and dust models are fixed. Parameters (AOD_{443} , k_0 , b) are derived simultaneously by matching the EPIC TOA reflectance at 340, 388 and 443 nm. The surface reflectance at these wavelengths is parameterized using the EPIC red band (680 nm) and their spectral ratios to the red band obtained for each 10 km grid cell using the minimum reflectance method. The variety of retrieved combinations
145 (k_0 , b) characterize the magnitude of aerosol absorption and its spectral variability. MAIAC retrievals are reported for the effective aerosol heights of 1 km and 4 km, representing the typical boundary layer and free troposphere transported aerosol. As current MAIAC EPIC cannot discriminate between smoke and dust, it uses the dust model for known dust source regions (e.g., Sahara, Arabian Peninsula etc.), and the smoke model is applied elsewhere globally. The lack of the mixed smoke-dust



aerosol types is a current limitation of the algorithm. The MAIAC EPIC version 2 reports the combination of AOD, k_0 and b along with calculated SSA at 443 nm. Our comparisons of SSA of MAIAC EPIC for 2018 for mineral dust with AERONET SSA showed an agreement with correlation coefficient $R \sim 0.62$, RMSE ~ 0.021 , and MBE ~ 0.006 over Sahara–Arabia–Middle East region, and with 85% of SSA values within expected error (EE) of ± 0.03 (Lyapustin et al., 2021). The global AOD and SSA accuracy analysis of EPIC MAIAC for the entire mission period 2015–2021 will be published elsewhere.

A comparison of spectral dependence of dust absorption ($\log(k_{440})$ vs $\log(k_{670})$) with AERONET showed a very similar pattern and slope, albeit MAIAC EPIC gave a smaller range of variation. Such good unbiased agreement was observed for dust at 1 km effective height, indicating that the bulk of dust for the majority of dust storms was in the boundary layer. On the contrary, a similar SSA validation for the wildfire smoke over the USA showed a much better agreement with AERONET for the lofted smoke at 4 km effective height (for 15 out of 17 AERONET sites, Lyapustin et al., 2021). For this reason, the current work uses MAIAC EPIC dust retrievals reported for the 1 km height.

160

2.2 Composition retrieval of hematite and goethite

The forward and inversion algorithms for hematite and goethite retrievals are illustrated in Fig. 2. The forward model uses the Maxwell–Garnett effective medium approximation to simulate complex dielectric function of the total column. Although internal mixing is clearly assumption for minerals, as minerals are generally externally mixed—other than iron oxides (hematite, goethite; Formenti et al., 2014a), ESMS within each particle mode and AERONET retrievals also assume internal mixing, so the retrieval can be directly fitted into ESMS or compared with AERONET data in the future.

The complex dielectric function (ε), the so-called relative permittivity, is equal to the square of the corresponding complex refractive index ($m^2 = (n + ik)^2$), where $\varepsilon_1, \varepsilon_2, \varepsilon_h$ indicate the complex dielectric functions of inclusion 1, 2, and the host, respectively:

170

$$\varepsilon_1 = \varepsilon_{1,r} + i\varepsilon_{1,i} = (n_1^2 - k_1^2) + i(2n_1k_1), \quad (2)$$

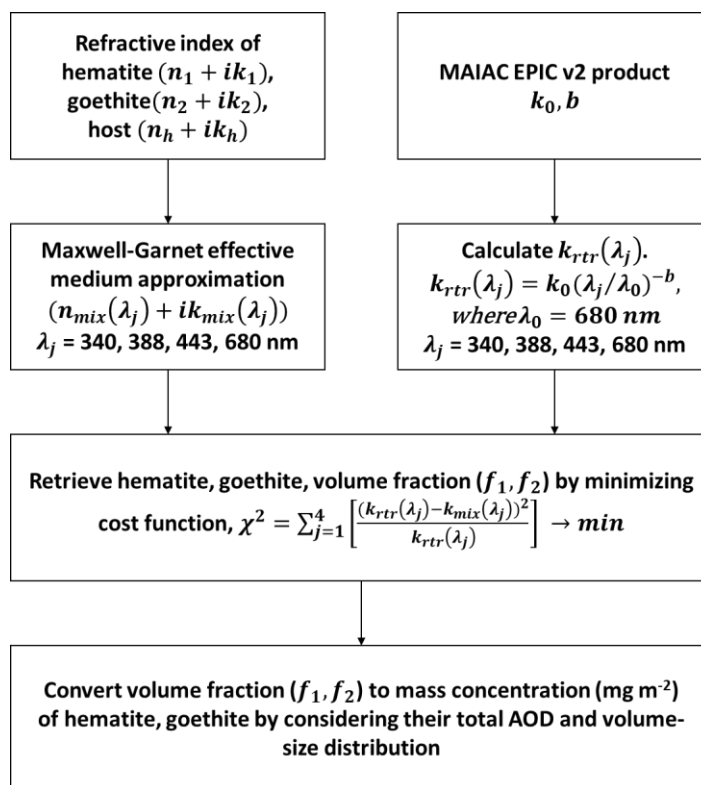
$$\varepsilon_2 = \varepsilon_{2,r} + i\varepsilon_{2,i} = (n_2^2 - k_2^2) + i(2n_2k_2), \quad (3)$$

$$\varepsilon_h = \varepsilon_{h,r} + i\varepsilon_{h,i} = (n_h^2 - k_h^2) + i(2n_hk_h). \quad (4)$$

Here, inclusions 1 and 2 refer to hematite and goethite, respectively, and the host is generally a homogeneous aerosol mixture whose absorption can be neglected ($k_h(\lambda_j) = 0$). This assumes that all absorption in mixed aerosols is attributed to hematite and goethite particles. The complex refractive indices of hematite and goethite were brought by Scanza et al. (2015) and Bedidi and Cervelle (1993), respectively, as depicted in Fig. 1 (Note that in Scanza et al. (2015) the complex refractive



index of hematite originally cited as personal communication with A. H. M. J. Triaud, 2005;
 180 <http://www.atm.ox.ac.uk/project/RI/hematite.html>). Here, we linearly extrapolated the goethite refractive index to 340 nm in
 the UV region. The real part of the refractive index of the host ($n_h(\lambda_j)$) is 1.52, 1.52, 1.51, and 1.5 at 340, 388, 443, and 680
 nm, respectively, as determined by Di Biagio et al. (2019).



185 **Figure 2: Schematic diagram of the methodology of this study. Spectral aerosol absorption data from MAIAC EPIC (b and k_0 values) are used to infer imaginary refractive indices (k_{rr}) at 340, 388, 443, and 680 nm. These values are fitted with imaginary indices of mixtures with hematite, goethite, and host complex refractive index using the Maxwell–Garnett effective medium approximation rule. The cost functions between the EPIC imaginary and mixture refractive indices are minimized by iteration of volume fractions (f) of hematite and goethite (Section 2.2).**

190 The complex dielectric function of mixed aerosol (ϵ_{MG}) can be summarized as follows using the Maxwell–Garnett effective medium approximation:

$$\epsilon_{MG} = \epsilon_h \left[1 + \frac{3 \left(f_1 \frac{\epsilon_1 - \epsilon_h}{\epsilon_1 + 2\epsilon_h} + f_2 \frac{\epsilon_2 - \epsilon_h}{\epsilon_2 + 2\epsilon_h} \right)}{1 - f_1 \frac{\epsilon_1 - \epsilon_h}{\epsilon_1 + 2\epsilon_h} - f_2 \frac{\epsilon_2 - \epsilon_h}{\epsilon_2 + 2\epsilon_h}} \right] = \epsilon_{MG,r} + i\epsilon_{MG,i} \quad (5)$$



195 where f_1 , f_2 refer to volume fractions (unitless) of inclusions 1 and 2, respectively. The volume fraction of the host is $(1 - f_1 - f_2)$. Therefore, the complex refractive index of the mixture is a function of two inclusions and one homogeneous host:

$$m_{mix}(\lambda_j) = F(f_1, f_2, m_1(\lambda_j), m_2(\lambda_j), n_h(\lambda_j)) = n_{mix}(\lambda_j) + ik_{mix}(\lambda_j) \quad (6)$$

200

where the real and imaginary parts of the aerosol mixture, derived from the relation $\varepsilon_{MG} = m_{mix}^2$, are:

$$n_{mix} = \sqrt{\frac{\varepsilon_{MG,r}^2 + \varepsilon_{MG,i}^2 + \varepsilon_{MG,r}}{2}} \quad (7)$$

$$k_{mix} = \sqrt{\frac{\varepsilon_{MG,r}^2 + \varepsilon_{MG,i}^2 - \varepsilon_{MG,r}}{2}} \quad (8)$$

205

The inversion minimizes the following cost function by iteratively updating the volume fraction of inclusions ($[f_1, f_2]$):

$$\chi^2 = \sum_{j=1}^4 \left[\frac{(k_{rtr}(\lambda_j) - k_{mix}(\lambda_j))^2}{k_{rtr}(\lambda_j)} \right] \rightarrow \min, \quad (9)$$

where

210

$$k_{rtr}(\lambda_j) = k_0(\lambda_j/\lambda_0)^{-b}, \text{ where } \lambda_0 = 680\text{nm}. \quad (10)$$

The parameter λ_j represents the four EPIC wavelengths of 340, 388, 443, and 680 nm. Unlike Schuster et al. (2016), we minimize only the imaginary term of the mixture refractive index. However, the real parts of the refractive indices of inclusions 1, 2, and the host are significant, as the imaginary term of the mixture ($k_{mix}(\lambda_j)$) is calculated from both real ($\varepsilon_{MG,r}$) and imaginary ($\varepsilon_{MG,i}$) parts of the complex dielectric function. Therefore, realistic values of the real part of the refractive indices of inclusions 1, 2, and the host are still required as well as those of the imaginary part. Di Biagio et al. (2019) concluded that the real part of the refractive index is generally source- and wavelength-independent with a range of 1.48–1.55 and a sample mean of 1.52, based on a study of 19 mineral dust and soil samples from different main global dust sources. As we mentioned above, we used the values 1.52, 1.52, 1.51, 1.5 at 340, 388, 443, 680 nm, respectively.

220 The retrieved volume fractions of hematite and goethite ($[f_1, f_2]$), can be converted to mass concentrations (mg m^{-2}) by considering their total AOD and volume–size distributions. Specifically, total AOD (τ^a) is a summation of the fine-mode



and coarse-mode AOD, with MAIAC considering fixed $h_i(\lambda)$ (AOD per unit volume concentration) values and C_{Vi} (volume concentration) for each mode (Lyapustin et al., 2011):

$$\tau^a = \tau_f^a + \tau_c^a = C_{Vf}h_f + C_{Vc}h_c \approx C_{Vc}h_c \quad (11)$$

225 For dust, MAIAC uses a dynamic model of size distribution for the Solar Village AERONET site (Dubovik et al., 2002). In this model, the volume fraction of the coarse mode rapidly increases with AOD. This justifies the approximation in (11) as MAIAC provides flexible (AOD, k_0 , b) retrievals only when the background model AOD is high (AOD > 0.6). A constant value of $h_c(443) = 1.2526$ for dust yields the following simple equation:

230
$$C_{Vc} = \tau^a / 1.2526 \quad (12)$$

The volume concentration of hematite ($C_{V,hema}$) can be obtained by multiplying the total volume concentration and retrieved volume fraction of hematite:

235
$$C_{V,hema} = C_{Vc} \times f_{hema} = \tau^a / 1.2526 \times f_{hema} \quad (13)$$

and the mass concentration of hematite ($C_{M,hema}$) is calculated by multiplying the corresponding densities ($\rho_{hema} = 5260 \text{ kg m}^{-3}$; $\rho_{goethite} = 3800 \text{ kg m}^{-3}$; $\rho_{host} = 2500 \text{ kg m}^{-3}$; Scanza et al., 2015):

240
$$C_{M,hema} = C_{V,hema} \times \rho_{hema} = \tau^a / 1.2526 \times f_{hema} \times \rho_{hema} \quad (14)$$

Accordingly, the mass concentration of goethite ($C_{M,goet}$) and host ($C_{M,host}$) can be calculated by replacing f_{hema} and ρ_{hema} in equation (13) and (14) with the corresponding volume fraction and density. Density of free iron is roughly twice that of other minerals (Schuster et al., 2016; Formenti et al., 2014a).

245

2.3 Hematite refractive index

The published values of laboratory-based spectral refractive indices of hematite in the 300-700 nm range are highly variable (Fig. 3; Table 1; Schuster et al., 2016; Zhang et al., 2015). Hematite is a uniaxial crystal with hexagonal structure. The optical functions of hematite (complex dielectric function ($\hat{\epsilon}$) or complex refractive index (m)) have been obtained in laboratory studies using techniques such as ellipsometry spectroscopy, which provides complex dielectric functions as a function of photon energy of ordinary and extraordinary rays (Chen and Cahan, 1981; Vernon 1962), reflectance spectra measurements



(Query, 1985; Sokolik and Toon, 1999; Bedidi and Cervelle, 1993), transmission and scattering measurements (Kerker et al., 1979; Hsu and Matijevic, 1985), diffuse reflectance measurements (Gillespie and Lindberg, 1992), and absorption coefficient measurements (Marusak et al., 1980). The refractive index of hematite also has been calculated by combining existing four measurements of Galuza et al. (1979), Kerker et al. (1979), Steyer (1974) and Onari et al. (1977) (Longtin et al., 1988).

Information on the complex refractive index of goethite is much more scarce, with two types of indices having been published by Bedidi and Cervelle (1993) and Glotch and Roman (2009) for 0.45–0.75 μm and 8–50 μm wavelength ranges, respectively. Hematite and goethite complex refractive indices (or dielectric functions) are needed for the UV–Vis region as *a priori* information for determination of the retrieved volume fraction of hematite and goethite by EPIC MAIAC (Section 2.2). We therefore examined how the volume fractions of hematite and goethite change with the different types of hematite refractive indices (Sections 2.3 and 4).

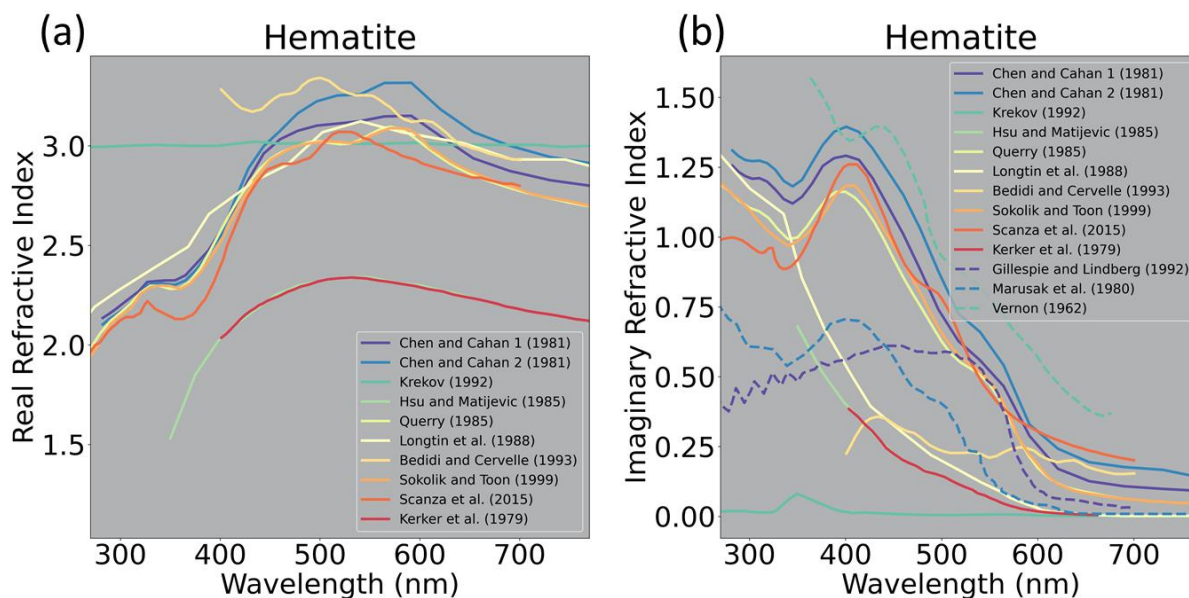


Figure 3: Plots of previously published hematite refractive indices at 300–700 nm: (a) real part; (b) imaginary part . The reference information is also summarized in Table 1.

265



Table 1: Summary of hematite refractive index information used in Fig. 3.

No.	Reference	Wavelength	Structure	Temperature	Method
1	Chen and Cahan (1981) –1*	263–770 nm	Polycrystalline (α -Fe ₂ O ₃)	1100°C	Ellipsometry spectroscopy (* the paper provided two samples sintered at different temperature)
2	Chen and Cahan (1981) –2*			1250°C	
3	Krekov (1992)	200–4500 nm	-	-	-
4	Gillespie and Lindberg (1992)	250–700 nm	Fe ₂ O ₃	-	Measure diffuse reflectance, using the dilution method of the Kubelka–Munk (K–M) diffuse reflectance theory
5	Hsu and Matijevic (1985)	350–650 nm	Colloidal hematite (0.10, 0.12, 0.13, 0.15, 0.16, 0.51 μ m)	25°C	Taken from Kerker et al. (1979)
6	Query (1985)	210–900 nm	Uniaxial Crystal (α -Fe ₂ O ₃)	-	Spectrophotometer, using Kramers–Kronig
7	Longtin et al. (1988)	200–300000 nm	Fe ₂ O ₃	-	Combining 4 measurements
8	Bedidi and Cervelle (1993)	350–750 nm	Hematite (Ordinary index)		Koenigsberger formula
9	Sokolik and Toon (1999)	200–50000 nm	-	-	Taken from Query (1985) (Based on clarification by Zhang et al. (2015))
10	Kerker et al. (1979)	400–880 nm (n) 400–700 nm (k)	α -Fe ₂ O ₃	-	n: Literature values of the average k: Measure transmission and scattered intensities, using Lorent–Mie theory of scattering by isotropic homogeneous spheres
11	Marusak et al. (1980)	207–945 nm	α -Fe ₂ O ₃	298K	Measure absorption coefficient
12	Vernon (1962)	350–700 nm	Single-crystal (α -Fe ₂ O ₃)	-	Ellipsometry spectroscopy
13	Scanza et al. (2015)	100–1000000 nm	Hematite	-	http://www.atm.ox.ac.uk/project/RI/hematite.html , cited as personal communication with A. H. M. J. Triaud, 2005

270

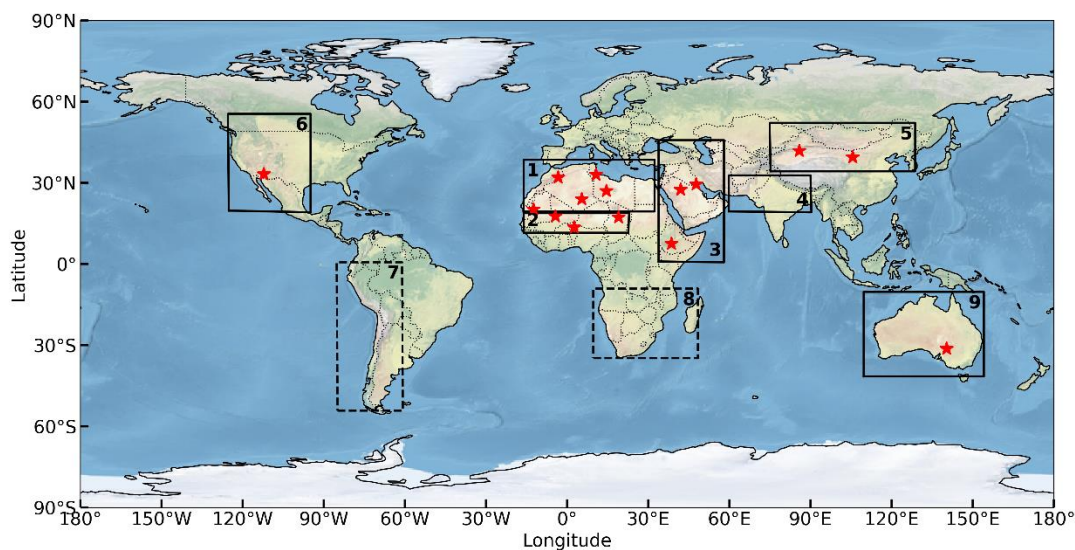
275



3 Results

280 Ginoux et al. (2012) described eight different global dust-source regions. We further divided the North Africa dust
source into two regions, northern Africa and the Sahel, following Di Biagio et al. (2017), and therefore considered a total of
nine different subcontinental dust-source regions (Fig. 4) including northern Africa (region 1), the Sahel (2), eastern Africa
and the Middle East (3), central Asia (4), eastern Asia (5), North America (6), South America (7), southern Africa (8), and
Australia (9). The MAIAC EPIC currently does not retrieve dust aerosol over regions 7 and 8. For regions 1–6 and 9, we
selected 24 significant dust events during 2015–2020 (Table 2; Fig. 5; Figs A1–A6; Fig. S1) for this study.

285



290 **Figure 4:** The nine main global dust source regions: (1) northern Africa, (2) the Sahel, (3) East Africa and the Middle East, (4)
central Asia, (5) East Asia, (6) North America, (7) South America, (8) southern Africa, and (9) Australia. From the eight regions
originally selected by Ginoux et al. (2012) North Africa was divided in northern Africa and the Sahel (Di Biagio et al., 2017). The
MAIAC EPIC version 2 does not provide dust aerosol data over regions 7 and 8 (square box of dashed line). The 15 red stars denote
soil locations of Di Biagio et al. (2019) where the soil properties were analyzed for the iron oxides content, complex refractive indices,
and SSA.



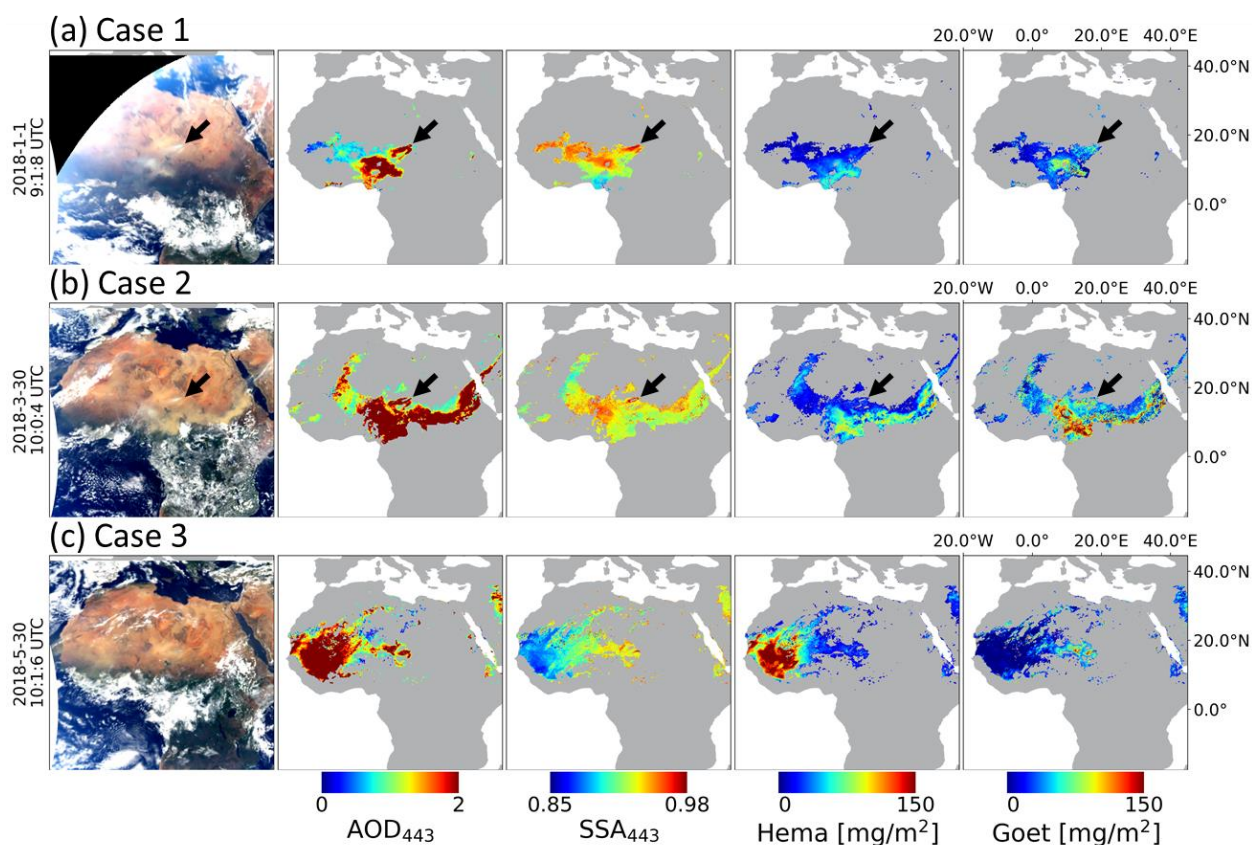
Table 2: Summary of information for selected dust episodes used in this study (Fig. 5; Figs A1–A6). Corresponding aerosol plume height (based on CALIOP) and volume size distribution (based on AERONET) are additionally presented in Fig. S1.

Case Num.	Geographical area	Event	Longitude: min, max	Latitude: min, max	Region
Case 1	Sahara–Sahel	January 1, 2018	–20.00, 46.00	–20.00, 43.00	Bodélé Depression
Case 2		March 30, 2018	–20.00, 46.00	–20.00, 43.00	Vast Dust over Sahara
Case 3		May 30, 2018	–20.00, 46.00	–20.00, 43.00	western Africa to Atlantic Ocean
Case 4		February 21, 2016	–13.35, –2.03	32.56, 42.33	Sahara to Portugal and Spain
Case 5		February 22, 2017	–5.90, 7.94	32.27, 41.27	Algeria to Spain
Case 6		August 6, 2015	22.32, 36.95	13.53, 27.39	Sudan toward southern Egypt
Case 7		August 7, 2015	22.32, 36.95	13.53, 27.39	Sudan–Egypt–Red Sea
Case 8	Middle East	September 1, 2015	39.69, 51.01	27.74, 37.40	Middle East (Iraq and Iran), Shamal, Haboob
Case 9		September 2, 2015	39.69, 51.01	27.74, 37.40	Middle East (Iraq and Iran), Shamal, Haboob
Case 10		September 7, 2015	34.45, 44.19	30.30, 37.93	Middle East (Iraq and Iran)
Case 11		July 28, 2018	41.69, 60.15	12.58, 25.56	Saudi Arabia
Case 12	India	May 3, 2018	62.00, 85.00	15.78, 35.59	India dust in Spring (pre–monsoon)
Case 13		May 14, 2018	62.00, 85.00	15.78, 35.59	India dust in Spring (pre–monsoon)
Case 14		June 14, 2018	62.00, 85.00	15.78, 35.59	India dust in Late Spring (pre–monsoon)
Case 15	East Asia	April 30, 2016	76.35, 90.59	30.96, 46.34	Taklimakan
Case 16		May 1, 2016	76.35, 90.59	30.96, 46.34	Taklimakan
Case 17		May 4, 2017	112.25, 121.35	35.72, 45.17	Gobi Desert to Russia
Case 18	North America	March 31, 2017	–109.04, –103.05	29.54, 35.94	Mexico–New Mexico
Case 19		March 31, 2017	–109.04, –103.05	29.54, 35.94	Mexico–New Mexico
Case 20		April 10, 2019	–108.66, –100.96	30.44, 37.6	Mexico–New Mexico
Case 21		April 10, 2019	–108.66, –100.96	30.44, 37.6	Mexico–New Mexico
Case 22	Australia	February 12, 2019	132.96, 153.70	–38.67, –20.11	Australia
Case 23		February 12, 2019	132.96, 153.70	–38.67, –20.11	Australia
Case 24		February 13, 2019	132.96, 153.70	–38.67, –20.11	Australia

3.1 Case studies

3.1.1 Northern Africa (Sahara) and the Sahel

Three different dust events over the Sahara and Sahel regions are depicted in Fig. 5, which are the same episodes illustrated by Lyapustin et al. (2021) in their Fig. 4. In winter (late November to mid-March), western Africa is known for its
300 northeasterly dry, dusty wind, the “Harmattan”. In summer, due to the Intertropical Convergence Zone (ITCZ) moving northward by $\sim 20^\circ\text{N}$ during July–August and returning south by January (close to equatorial over western Africa; Nicholson, 2018), there is a southwesterly humid monsoon flow from the Gulf of Guinea over the low West African Sahelian area (Formenti et al., 2011b).



305

Figure 5: Dust episodes over Sahara–Sahel region. From left, RGB TOA image generated from EPIC L1B version 3 data, MAIAC AOD and SSA at 443 nm, hematite and goethite mass concentrations for January 1, 2018 (top); March 30, 2018 (middle); May 30, 2018 (bottom). The black arrows point at the Bodélé Depression area.



310 The topmost row in Figure 5 shows the Bodélé Depression episode of January 1, 2018. In Chad, this is known as the
largest single dust source with the low iron-oxide content (~ 0.7 wt.%; Di Biagio et al., 2019) due to the diatomaceous sediments
of the region (Todd et al., 2007; Moskowitz et al., 2016). On that particular day, the AOD_{443} was high at ~ 2.0 over the Bodélé
Depression; there was negligible hematite mass concentration and up to 75 mg m^{-2} goethite mass concentration, corresponding
to $0.5\text{--}1$ wt.% iron-oxide near the source regions by our calculation (not shown), consistent with the 0.7 wt.% of Di Biagio et
315 al. (2019). Immediately south of Bodélé, a different dust source was active with higher hematite concentration judging by its
reddish color compared with the white dust from the Bodélé Depression.

Second row in Figure 5 illustrates another dust event of March 30, 2018, with typical values of dust 443 nm SSA of
 ~ 0.92 . This event began on March 28 near the central Sahara and spread to the Sahara and Sahel regions where it persisted for
about a week, moving south before spreading to the southwest. During these events, our retrieval shows a variable hematite
320 concentration of $75\text{--}100 \text{ mg m}^{-2}$, with higher goethite mass concentrations of $75\text{--}150 \text{ mg m}^{-2}$ in some areas. This trend towards
goethite predominance over hematite in the Sahara and Sahel regions is consistent with the findings of Lafon et al. (2006) and
Formenti et al. (2014a), although our results pertain to late March while the former and latter other studies were laboratory
generated from soil and in summer or winter, respectively. In the analysis by Formenti et al. (2014a), the goethite content of
iron oxides was $52\text{--}78$ wt.%, with the highest values being for dust originating in the Sahel. Our analysis is showing a similar
325 range (over 50 wt.%) of goethite in iron oxides in this event.

The third row in Fig. 5 shows dust events with high hematite contents and highly absorbing ($SSA_{443} \sim 0.87$) properties
over the western Sahara on May 30, 2018. Visual analysis indicates that the dust originated in the western Sahara over Algeria
and Mali on May 27, and was transported by northeasterly winds towards the western Sahel, and then on to the Atlantic Ocean.

Another dust case over northern Africa is shown in Fig. A1, with the top row (February 21, 2016) depicting dust
330 blown northward from the Sahara to Portugal and Spain by the Calima, a warm southeasterly wind common in North Africa
in winter. On the same day, AERONET measurements at the Valladolid site in Spain detected a coarse-mode aerosol with
 SSA_{443} of ~ 0.875 to ~ 0.925 (Fig. S1), similar to the MAIAC EPIC SSA recorded over Spain. The second row (February 22,
2017) also depicts dust events involving Calima transport from Algeria to Spain. On that particular day, AERONET at the
Granada site in Spain detected the coarse-mode size distribution with SSA_{443} of ~ 0.90 , similar to the MAIAC-retrieved SSA
335 value of ~ 0.90 . The Calima often carries dust to the Canary Islands, although the atmospheric low-pressure systems may
deflect the winds northward. On February 22, 2017, the Cloud-Aerosol Lidar with Orthogonal Polarization (CALIOP) detected
dust aerosol mostly at $2\text{--}4 \text{ km}$ (Fig. S1) above southern Spain. Both the first- and second-row cases in Fig. A1 involved the
Calima wind and demonstrated hematite transport to the Iberian Peninsula, whereas goethite transport was negligible.

The third (August 6, 2015) and fourth (August 7, 2015) rows of Fig. A1 describe dust transport north from the Sudan
340 toward southern Egypt near Aswan, which is clearly visible in red-green-blue (RGB) images generated with TOA reflectance.
On both these days, the SSA value of the plume as determined by MAIAC was slightly below 0.92 , the typical dust SSA value.
Ginoux et al. (2012) described this area as the “Nile River Basin”, containing essentially natural sources. Prospero et al. (2002)



determined that dust sources over Egypt become active during March–October. Our retrieval results indicate that the iron oxides there comprised mainly hematite with a spatial distribution similar to that of the plume AOD₄₄₃.

345 3.1.2 Middle East

Selected dust cases over the Middle East are shown in Fig. A2, where the top two rows (September 1 and 2, 2015) represent the general characteristics of the Shamal, with hot and dry northwesterly winds blowing towards the Persian Gulf in summer, including the Haboob wind. This dust event was triggered on August 31 by a surface low-pressure system on the Syria–Iraq border, moving across Iraq, Iran, and the Persian Gulf region over the next two to three days. The first row
350 (September 1) in Fig. A2 depicts a cyclone-shaped dust storm with AOD₄₄₃ > 2 and a moderately absorbing SSA₄₄₃ value (~0.92). Hematite was located more toward the center of the cyclone, whereas goethite was distributed within its tail, toward the east-southern part of the cyclone core. On September 2 (Fig. A2, second row), the dust storm moved towards the coastline near the Persian Gulf with consistent AOD₄₄₃ and SSA₄₄₃ values of ~2 and ~0.92, respectively. However, the reduced spectral absorption exponent b with a slightly increased k_0 value indicates a change in chemical composition (not shown). The cyclone
355 appears to have a higher goethite content than hematite in its core. Note that both first row and second row in Fig. A2 are observed at 6:50 UTC and 6:59 UTC, respectively. Therefore, the changed chemical composition are not likely affected by geometry dependency of the MAIAC EPIC (b , k_0) retrieval algorithm.

Fig. A2, third row (September 7, 2015), shows the dust first emerging on September 6 near the Euphrates River in Syria. By September 7 the dust had engulfed Syria, northern Jordan, and southern Turkey over the Mediterranean coast. On
360 September 7, the Sede Boker AERONET site in southern Israel detected a coarse-mode dominant volume–size distribution and corresponding SSA of 0.89–0.92 (Fig. S1). By September 9, the dust had moved southwest over northeastern Egypt, and Sede Boker AERONET site detected AOD₄₄₃ > 2.75. Ginoux et al. (2012) described this source region as comprising ‘anthropogenic’, ‘natural’, and ‘hydrologic’ aerosol, and named it the ‘Mesopotamia source’, which is most active during June–August. Ginoux et al. (2012) considered it ‘natural’ if <30% of the area was agricultural; otherwise it was ‘anthropogenic’
365 (>30% agricultural). If the dust-event incidence is associated with ephemeral water bodies, the source is termed ‘hydrologic’. For the Euphrates River area, farmland northeast of the city of Ar Raqqa in Syria has the most frequently active anthropogenic dust sources (Walker et al., 2009), and several salt-flat areas near the Iraq–Syria border are significant natural dust sources (Ginoux et al., 2012). Our retrieval results indicate that on September 6, hematite was predominant northeast of Ar Raqqa, but on September 7 (third row, Fig. A2) the goethite content was predominant, likely owing to different land use (Fitzpatrick,
370 2004; Journet et al., 2014).

The Fig. A2, fourth-row, episode (July 28, 2018) describes another dust event in the Shamal over the Rub’al Khali sandy desert area. This event swept across the Arabian Peninsula during July 27–28, with a swirling cyclone shape over part of the Persian Gulf, Gulf of Oman, Arabian Sea, and Gulf of Aden during July 29–30. Near this dust-storm region, there are two dust sources (Ginoux et al., 2012), the ‘Empty Quarter’ and ‘highlands of Saudi Arabia’. The former refers to a salt-flat



375 region named ‘Sabkha Matti’ on the border between the United Arab Emirates and Saudi Arabia. The latter lies in the northern
Rub’al Khali sandy desert area, which comprises three dry riverbeds (Ginoux et al., 2012). Our chemical-composition retrieval
results (Fig. A2) indicate a hematite-dominated distribution overall but mixed with goethite along the coast of Oman.

3.1.3 Central Asia (India)

380 A dust event over India is depicted in Fig. A3. Large amounts of dust were observed during the pre-monsoon season
of March–May over northern India, with the lowest dust incidence in the post-monsoon season of September–November
(Ginoux et al., 2012). Pre-monsoonal dust storms are attributed primarily to the Arabian Peninsula and the Thar desert, with
wind transport to northwestern India (Sarkar et al., 2019). Three 2018 dust storms (Fig. A3) swept across the Rajasthan and
Uttar Pradesh regions by westerly or southwesterly winds from western India. The Himalayan mountain region blocks dust
movement further north and usually deflects transport eastward.

385 Fig. A3, row one (May 3, 2018) indicates dust with AOD₄₄₃ values of 1–2 near Rajasthan with an SSA₄₄₃ value of
~0.92. Despite the uniform SSA over the aerosol plume, our compositional retrieval results indicate that hematite was
predominant in the northern part of the plume, with goethite occurring only in that part over the Thar Desert near to the border
with Pakistan or over coastal areas of western India.

390 One week later (row two, May 14, 2018) and a month later (row three, June 14), the same Rajasthan region suffered
severe dust storms again, with these being recorded as anomalously intense dust storms. In the latter event, dust was trapped
over northern India by southerly winds from the Bay of Bengal. In both cases, hematite was concentrated more towards the
center of the plume, with concentrations of >100 mg m⁻², whereas the goethite content was small (<50 mg m⁻²).

395 The Kanpur region of northern India may have aerosol properties reflecting mixtures of pollution aerosol from the
combustion of fossil fuels and biofuels, and desert dust (Eck et al., 2010). During the events depicted in Fig. A3, the AERONET
inversion data (version 3, level 2) for Karachi (northwestern coast of India) indicated coarse-mode dominant size distribution
on May 3 and 14 (rows two and three, Fig. A3) with SSA values of ~0.9 (Fig. S1), whereas in the Kanpur region (northern
India) small bio-modal size distributions were detected (fine/coarse volume–size distribution peak 0.04/0.18 on May 3;
0.12/0.42 on May 13; 0.05/0.46 on June 14). This implies that dust aerosol might have been mixed with fine-mode pollution
aerosol over northern India. Our retrieval algorithm currently fits only the pure dust model, so the retrieved hematite and
400 goethite concentrations may be biased in this case.

3.1.4 East Asia

405 In East Asia, there are two main regional sources of mineral dust, the Taklimakan and Gobi deserts. Fig. A4 (first and
second rows) illustrates a Taklimakan Desert dust event in spring (April 30 and May 1, 2016). During this event, dust was
transported by easterly winds and circulated clockwise around the Tarim Basin for two days. The Tarim Basin is flanked by
~5-km-high mountain ranges to the west, south, and north; therefore, dust storms usually blow in from the east at low levels,



trapping the event in the basin. Strong surface winds may carry dust to altitudes of ~10 km, transporting it across China and the Pacific Ocean. On April 30, 2016, a severe dust event ($AOD_{443} \sim 2.0$) with SSA_{443} values of ~0.90 displayed hematite predominance over goethite at 07:27 UTC. Over the next two days, the SSA_{443} increased to ~0.95 with the reduced hematite content, while goethite content increased slightly to 50–60 $mg\ m^{-2}$.

410 Fig. A4, row three, describes a dust event originating in the Gobi Desert with dust being transported to Russia over East Asia. This event was pushed by a cold front over the Gobi Desert near the border of China and Mongolia and was clearly captured by MODIS Aqua on May 3, 2017 (not shown). On May 4, the dust moved to the Russian border just east of Mongolia in a cyclonic circulation, bypassing the Beijing area. The AERONET sites in Beijing (Fig. S1), Beijing_RADI, and XiangHe detected coarse-mode dominant volume–size distributions with SSA values of ~0.91 on May 4, implying pure dust aerosol.
415 Our algorithm retrieved moderate goethite concentrations (~75 $mg\ m^{-2}$) with low hematite concentrations (<50 $mg\ m^{-2}$).

3.1.5 North America

Dust events over North America near the White Sands in New Mexico are illustrated in Fig. A5, for March 31, 2017 (first and second rows) and April 10, 2019 (third and fourth rows). The highest frequencies of dust event over North America occur in the southwestern USA and northern Mexico at up to 30% of the time in spring (Ginoux et al., 2012). However,
420 MAIAC EPIC version 2 does not retrieve dust aerosol over the southwestern USA, so only northern Mexico events are considered here.

On March 31, 2017 (first and second rows, Fig. A5), MAIAC captured dust patterns changing hourly in the southern White Sands area. The likely dust source was the Chihuahuan Desert near the border of Mexico and New Mexico, south of El Paso International Airport or near Janos in Mexico (based on MODIS RGB images not shown here). In both the March 31
425 cases, the goethite concentration was not much (<50 $mg\ m^{-2}$). Hematite was also rare at 19:05 UTC (first row) with $AOD_{443} < 1.0$ and $SSA_{443} \sim 0.91$, but reached 50–75 $mg\ m^{-2}$ at 20:53 UTC (second row), increasing to $AOD_{443} > 1.5$ and $SSA_{443} < 0.91$.

The April 10, 2019, dust storm was induced by a low-pressure meteorological system. Winds lofted dust from several sources around the region, including the White Sands area, Lordsburg Playa in southwestern New Mexico, the Chihuahuan Desert, and near the border of Mexico and New Mexico. In Fig. A5 (third and fourth rows), the white circle of the White Sands
430 is located near the center of the RGB image. Dust storms passed to the southeast of that area with moderate hematite contents (50–75 $mg\ m^{-2}$) and small goethite contents (<50 $mg\ m^{-2}$).

3.1.6 Australia

Australia often referred to as the “red continent” (Viscarra Rossel et al., 2010), with highly absorbing dust aerosols (Di Biagio et al., 2019). In Fig. A6, the first (February 12, 2019; 03:44 UTC) and second (05:32 UTC) rows depict a dust event
435 near Lake Eyre and Lake Blanche, both salt lakes in central South Australia—an area considered the ‘Lake Eyre Basin’, which is the most active dust source in Australia (Ginoux et al., 2012). Hourly EPIC RGB images indicate that the event started on

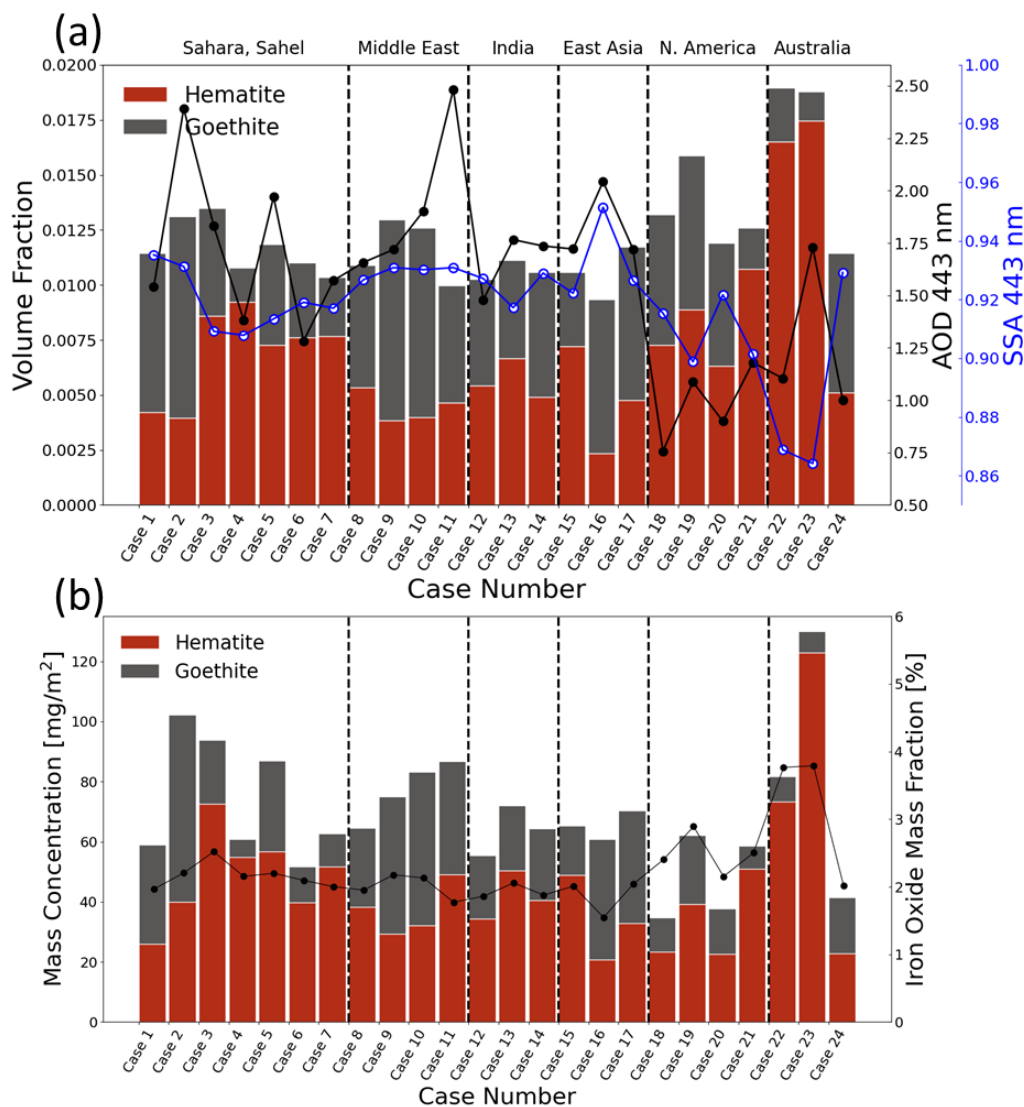


February 12 at 01:56–03:44 UTC (not shown). On that day, the AERONET sites at Birdsville (25.9°S, 139.3°E), in the northwest of the dust plume, detected coarse-mode-dominant volume–size distribution with $SSA_{443} \sim 0.82$ at 07:23 UTC (Fig. S1). Our retrieval results ($SSA_{443} < 0.85$) indicate high hematite concentrations, attributable to the iron-rich soils in the region.

440 On February 13 (row three, Fig. A6), the dust likely left-over from the previous day kept moving by southwesterly wind. The CALIOP instrument detected dust aerosol over eastern Australia at 32°–26°S at 0–3 km height (Fig. S1). The northern part of the dust plume might had passed the source of Simpson Desert, where dust activity is most frequent in the austral spring and summer (Ginoux et al., 2012). Overall, hematite was predominant over the area with $AOD_{443} > 1.5$.

3.1.7 Summary plot of the case studies

445 The 24 cases described here are summarized in Fig. 6. Over the Sahara, Sahel, and the Middle East, the iron-oxide volume fractions are comparable with those over North America, but the high AOD_{443} values yield higher mass concentrations than those in North America. Although Australia had lower AOD_{443} values than those of Sahara, Sahel and Middle East, the high volume fraction equated with high mass concentrations of hematite. The mass concentration of iron-oxide was relatively low over India, East Asia, and North America. Fig. 7 shows the relationship between iron-oxide mass fraction, SSA_{443} , and
450 imaginary refractive index at 443 nm. The previous study of Di Biagio et al. (2019) and Moosmüller et al. (2012) dealt with this relationship to estimate the spectrally resolved SW absorption of dust based on composition. Our retrievals were consistent with results of Di Biagio et al. (2019) in the relationship between iron-oxide mass fraction and SSA_{443} , but showed discrepancy in the relationship between iron-oxide mass fraction and imaginary refractive index at 443 nm likely due to the use of spherical particle shape in Di Biagio et al. (2019) calculation of imaginary refractive index (Kalashnikova and Sokolik, 2004).



455

Figure 6: Bar plot for the 24 cases described in Section 3.1. Case numbers for each row from Fig. 5, Figs A1–A6 are shown on the x axis and summarized in Table 2. (a) Mean volume fractions of hematite (red) and goethite (dark gray). Black and blue points show the corresponding mean AOD (right axis) and SSA at 443nm for each case. (b) Mean mass concentrations of hematite (red) and goethite (dark gray). Black points indicate corresponding iron-oxide mass fraction (wt.%; right axis) of total dust concentration.

460

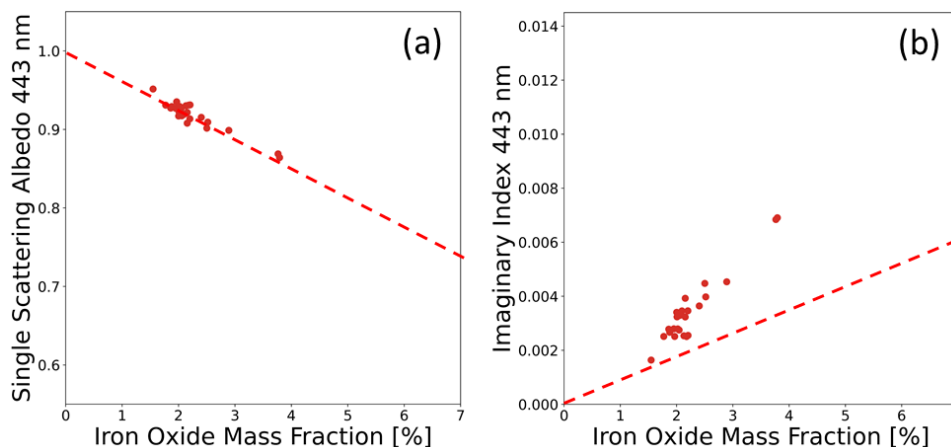


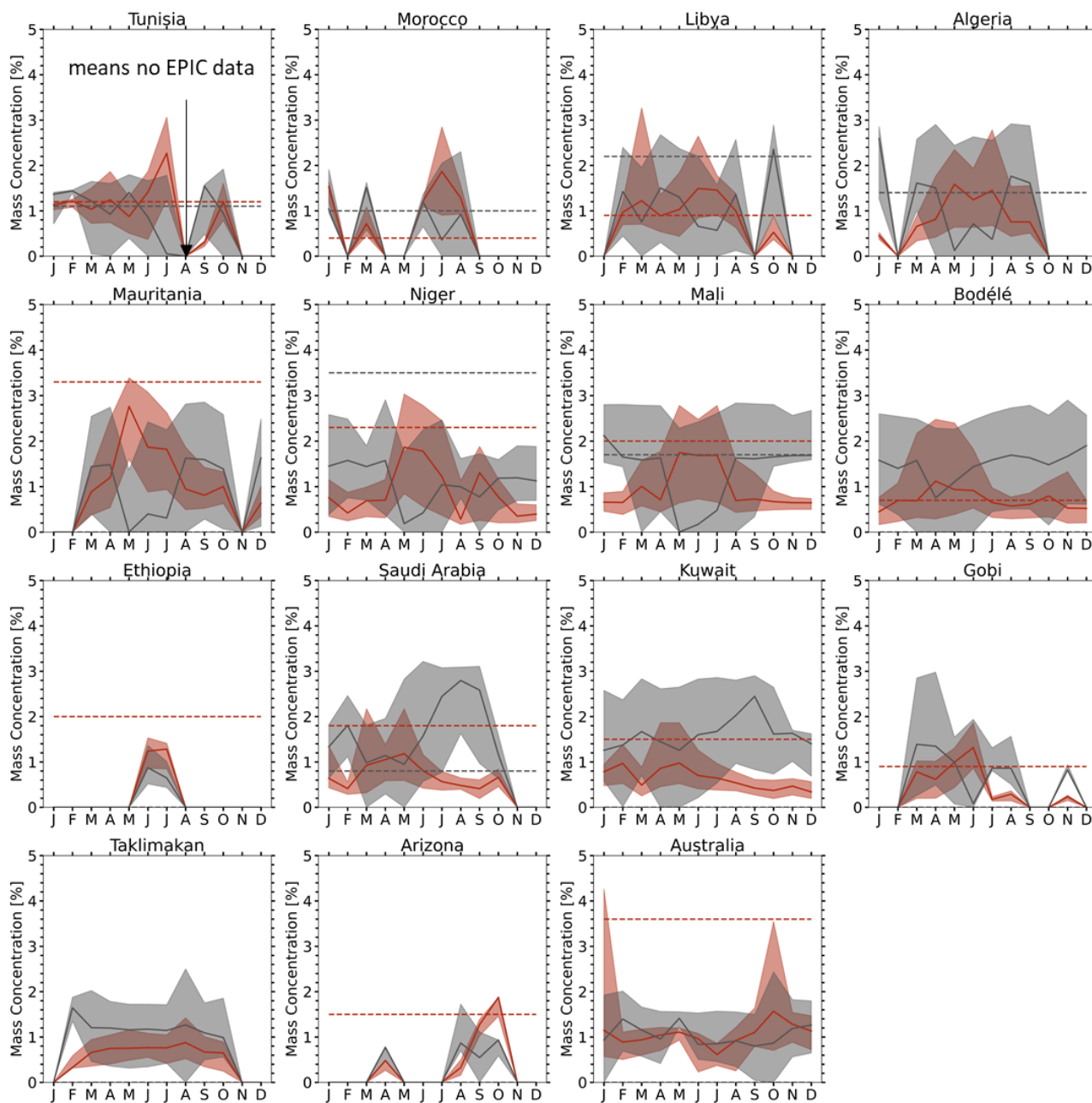
Figure 7: Relationship between iron-oxide mass fraction (wt.%; x axis) and SSA 443 nm (y axis, (a)) and imaginary refractive index (y axis, (b)). Red points represent the mean values of the 24 cases described in Section 3.1. Dashed line shows the estimated relationship at 443 nm from Di Biagio et al. (2019).

465

3.2 Comparison with *in situ* measurements of soil samples

Di Biagio et al. (2019) collected soil samples from 19 main dust sources representing global dust optical properties and determined their hematite and goethite contents by the X-ray absorption near-edge structure (XANES) method, providing bulk compositions of pure dust aerosol in dry conditions with a size range of 2–6 days of transport following emission. We compare their measured soil hematite and goethite mass concentrations (wt.%) with our retrieval results over 15 sites in Fig. 8 (for statistics, see Table S1). Only satellite-data pixels with $AOD_{443} > 1.0$ were used in the monthly composite, as some pixels of goethite retrieval with $AOD_{443} < 1.0$ display “noise” or “blob” patterns (e.g., third and fourth rows, Fig. A1). This noise may be attributed to their low signal to noise ratio with low AOD.

In Fig. 8, Tunisia (33.02°N, 10.67°E) and Morocco (31.97°N, 3.28°W) represent northern Africa, Libya (27.01°N, 14.50°E) and Algeria (23.95°N, 5.47°E), represent the central Sahara, Mauritania (20.16°N, 12.33°W) represents western Africa above the Sahel latitude (~20°N), Niger (13.52°N, 2.63°E), Mali (17.62°N, 4.29°W) and Bodélé (17.23°N, 19.03°E) represent the Sahel, Ethiopia (7.50°N, 38.65°E) represents eastern Africa, Saudi Arabia (27.49°N, 41.98°E) and Kuwait (29.42°N, 47.69°E) represent the Middle East (especially the Arabian Peninsula), Gobi (39.43°N, 105.67°E) and Taklimakan (41.83°N, 85.88°E) represent East Asia, Arizona (33.15°N, 112.08°W) represents North America, and Australia (31.33°S, 140.33°E) is represented by sites near Lake Eyre in central South Australia. The locations of all of the above are shown in Fig. 4.



485

Figure 8: Monthly variations (5th, 50th, and 95th percentiles) of hematite (red shading) and goethite (gray shading) mass concentration (wt.%) calculated from MAIAC EPIC at each site for 2018. Solid lines at the centers of shaded areas indicate median values for hematite (red) and goethite (black). Each site represents the area of $\pm 1^\circ$ of MAIAC EPIC data (pixel with AOD > 1.0) except for Australia ($\pm 3^\circ$). Dashed lines indicate hematite (red) and goethite (black) mass concentrations with $\pm 10\%$ uncertainty (Di Biagio et al., 2019). At the Algeria site, the two dashed lines coincide (Di Biagio et al., 2019). The invisible dashed lines of goethite (black dashed line) at Mauritania, Bodélé, Ethiopia, Kuwait, Gobi, Arizona and Australia indicate zero goethite mass concentration. Di Biagio et al. (2019) does not provide data at Taklimakan site. Monthly variations statistics are additionally presented in Table S1.



490 Although Di Biagio et al. (2019) collected data in each origin, the EPIC-retrieved hematite and goethite data may represent both local erosion and transported iron oxides, and these datasets may differ owing to seasonally and spatially varying dust transport from the different sources. Overall, however, our retrieved data tend to cover their entire range of hematite and goethite mass concentrations, except for the Niger site.

495 **3.2.1. Characteristics over northern Africa and the Sahel – Libya, Algeria, Mauritania, Niger, Mali, and Bodélé**

Sites in the central Sahara and Sahel, such as Libya, Algeria, Mauritania, Niger, Mali, and Bodélé, and in the Middle East such as Saudi Arabia and Kuwait, exhibit greater temporal variability than other sites, implying large dynamic dust-source variability in the Sahara, Sahel, and Middle East.

In the Sahara and Sahel, goethite is usually the predominant iron-oxide species by mass (Di Biagio et al., 2019; Lafon et al., 2006; Formenti et al., 2014a, b), as also indicated partially by our results. At four sites (Mauritania, Niger, Mali, and Bodélé) in the Sahel, goethite predominated over hematite during August–April, which included the Harmattan period. However, in early summer (May–July), the median hematite value was higher than that of goethite at these four sites, with higher hematite concentrations in the western Sahel peaking in May (Mauritania, ~2.9 wt.% > Niger, ~2 wt.% > Mali, ~1.8 wt.% > Bodélé, ~1.2 wt.%). The soil analysis data of Di Biagio et al. (2019) displayed a similar trend (Mauritania, 3.3 wt.% > Niger, 2.3 wt.% > Mali, 2.0 wt.% > Bodélé, 0.7 wt.%). Formenti et al. (2011a) and Lazaro et al. (2008) found that hematite is likely to predominate over goethite. Lazaro et al. (2008) detected hematite to goethite ratios of 0.5–2.0 in the Canary Islands, sourced from chotts in Tunisia and Northern Algeria (PSA NAF-1) and foothills of the Atlas Mountains in western Sahara and western Mauritania (PSA NAF-2), and the Mali region. Lazaro et al. (2008) also found hematite to goethite ratios of >1.0 in samples from February, March, May, August, September, and December, and ratios of <1.0 in January, February, June, August, and September. Schuster et al. (2016) described a maximum volume percentage of iron oxides associated with hematite ($H = V_{\text{hem}} / (V_{\text{hem}} + V_{\text{goe}}) \times 100$) of 83%–93% (median volume percentage of iron oxides associated with hematite of 38%–58%) over western Africa for pure dust cases, with the calculated percentage depending on hematite refractive index. The high-hematite dust regions are thus likely to exist in Mauritania, Niger, Mali in summer.

515 **3.2.2. Tunisia, Morocco**

In Tunisia, the median values of monthly composite of hematite and goethite are similar to those of Di Biagio et al. (2019; hematite, 1.2 wt.%; goethite, 1.1 wt.%) during January–May and in October, with retrieval values of ~1.2 wt.% for both. Data for the Morocco sites also agree well with those of Di Biagio et al. (2019) in March (hematite, 0.4 wt.%; goethite, 1.0 wt.%). However, the hematite concentration (~2 wt.%) was overestimated relative to soil data during June–August over both Tunisia and Morocco. Li et al. (2021) mentioned that hematite content in soil climatology J2014 (Journet et al., 2014) exhibits strong regional differences with mass fractions predominantly below 1.5 wt.% but reaching up to 5.0 wt.% in some arid regions such as over northern Africa. Total iron oxides mass concentrations vary over the range about 2–6.5 wt.% globally (2–5 wt.% of



Linke et al. (2006); 2.8–6.5 wt.% of Schuster et al. (2016)), meaning that hematite may be dominant in soil over some parts of northern Africa. Our results for Tunisia and Morocco are thus likely to occur in northern Africa.

525

3.2.3. Niger

Niger, in the central Sahel, lies downwind of some of the most persistent Saharan dust sources, including the Bodélé Depression in Chad, areas in northern Mali and southern Algeria, and also areas of Libya, Egypt, and the Sudan (Formenti et al., 2014a). Our median concentration of hematite (~2 wt.%) in May is consistent with that of Di Biagio et al. (2019; 2.3 wt.%), but goethite was underestimated (<1.8 wt.%; cf. 3.5 wt.% for Di Biagio et al., 2019). The goethite value of Di Biagio et al. (2019) corresponds to our highest value for monthly composite data for January–June (not shown). For Niger, Lafon et al. (2004) found iron-oxide concentrations of 2.8 ± 0.8 wt.% during the Harmattan season (November–March), with a major source being Bodélé in the Chad basin, whereas concentrations of 5.0 ± 0.4 wt.% were detected during the local erosion season (May–July). Our retrieval was consistent with the 2.8 wt.% value for the Harmattan season, but underestimated the local erosion season value. The Niger soil sites were close to the Banizoumbou AERONET site. MAIAC EPIC retrievals were in good agreement in accuracy with AERONET data for 2018 at this site, with AOD₄₄₃ (R, 0.8; RMSE, 0.23; MBE, -0.11) and SSA₄₄₃ within 0.03, 89% of samples and all within 0.05. Therefore, it is not likely the mixture aerosol type or the MAIAC AOD, SSA retrieval accuracy problem. AERONET direct AOD measurement data at Banizoumbou included only five days of measurement data in June, and most AOD values in July were <0.6 because of the May–October rainy season (with most rain in July–August). Our retrievals might not have detected iron oxides due to the low June–July AOD.

530
535
540

3.2.4. Bodélé

The Bodélé area is known to have low iron-oxide concentrations due to the presence of diatomic sediments (Todd et al., 2007; Moskowitz et al., 2016), and the high incidence of high-aerosol events is associated with the Venturi effect of Harmattan winds passing between the Ennedi and Tibesti mountains (Ginoux et al., 2012). The median hematite concentration was consistently low (<1.4 wt.%) over the whole of 2018, consistent with the value (0.7 wt.%) recorded by Di Biagio et al. (2019). Moreover, Moskowitz et al. (2016) concluded that dominant goethite and subordinate hematite together compose about 2 wt.% of iron oxides from the Bodélé Depression, similar trends with our data throughout the year. Iron-oxide levels over Bodélé (<2 wt.%) are shown later in Fig. 9, highlighting different areas especially in winter season, with a consistently high AOD average.

545
550

3.2.5. Ethiopia

The Ethiopia sites of Di Biagio et al. (2019) are near the Abidjatta–Shalla National Park. We occasionally detected dust over this area in June, with 150 pixels, and with <25 pixels in July. In June, median EPIC hematite value was ~1.2 wt.%, below the 2 wt.% indicated by soil measurement data.

555



3.2.6. Saudi Arabia, Kuwait

The hematite concentration at Saudi Arabia (median ~1.2 wt.% in May) was generally higher than that at Kuwait (~1 wt.% in February and May), consistent with the results of Di Biagio et al. (2019), with 1.8 wt.% in Saudi Arabia and 1.5 wt.% in Kuwait. In Saudi Arabia, the soil goethite content was 0.8 wt.%, similar to our retrieval during March–May (~1 wt.%). Both sites were dominated by goethite during summer–autumn (July–September). Summer and early autumn is the Shamal season when northwesterly winds blow over the Saudi Arabia peninsula (Yu et al., 2016), with the Saudi Arabia and Kuwait sites (Fig. 8) lying downwind. Therefore, transported dust by the Shamal might have caused the increase in dust goethite content.

3.2.7. Taklimakan, Gobi

Over East Asia, the Gobi Desert dust area was active mainly in April in our retrieval (with ~300 pixels), while the Taklimakan was active throughout the spring, early Summer, and September, all with >500 pixels of retrieval. In April, our hematite retrievals were consistent with data of Di Biagio et al. (2019), ~1 wt.% and 0.9 wt.%, respectively. Lafon et al. (2004) measured iron-oxide concentrations of ~3.7 wt.% downwind of Gobi Desert, but our median value even in April seems to underestimate that value. However, our retrievals were generally consistent with the hematite to goethite ratio by mass (~0.55) found by Shen et al. (2006) who investigated hematite to goethite mass-concentration ratios in bulk samples of eolian dust over Dunhuang (40.3°N, 94.5°E), Yulin (38.2°N, 109.4°E), and Tongliao (43.1°N, 122.1°E), yielding values of 0.57 ± 0.26 , 0.59 ± 0.16 , and 0.46 ± 0.13 , respectively.

3.2.8. Arizona and Australia

Both the Arizona and Australia sites may include significant smoke-event effects causing the increase of aerosol absorption that was attributed to the hematite content in our retrieval shown in Fig. 8. However, our case studies over North America (case 18–21) and Australia (case 23) presented in Fig. 6(b) cover the range suggested by Di Biagio et al. (2019) which is 1.5 wt.% (North America) and 3.6 wt.% (Australia) of soil measurement hematite content. Further study is needed to distinguish between smoke and dust in MAIAC EPIC algorithm.

Our retrievals thus generally follow the trends in hematite data recorded by Di Biagio et al. (2019) with some differences, especially for goethite likely associated with transport from different sources over the designated sites.

3.3 Global climatology

Seasonal average EPIC data for Sahara–Sahel and Middle East (Fig. 9) and Asia (Fig. 10) are shown for the period January 1 to December 31, 2018 (for global data, see Fig. S2–S5). As in Fig. 8, pixels of AOD > 1.0 were used to compute the average. Currently, MAIAC EPIC cannot differentiate between the smoke and the dust. It is mostly biomass burning smoke in the Indo-Gangetic plane (in Fig. 10) except during the pre-monsoon season, although there is also a dust from Thar desert. Also, part



of the data over North America and Australia (in Fig. S4, Fig. S5) may include some mixed aerosol or smoke cases, and thus
590 may be biased relative to pure-dust cases (Fig. 5; Figs A1–A6). Therefore, the results in the aforementioned region should not
be considered as accurate. Nevertheless, our results display the generally known iron-oxide patterns.

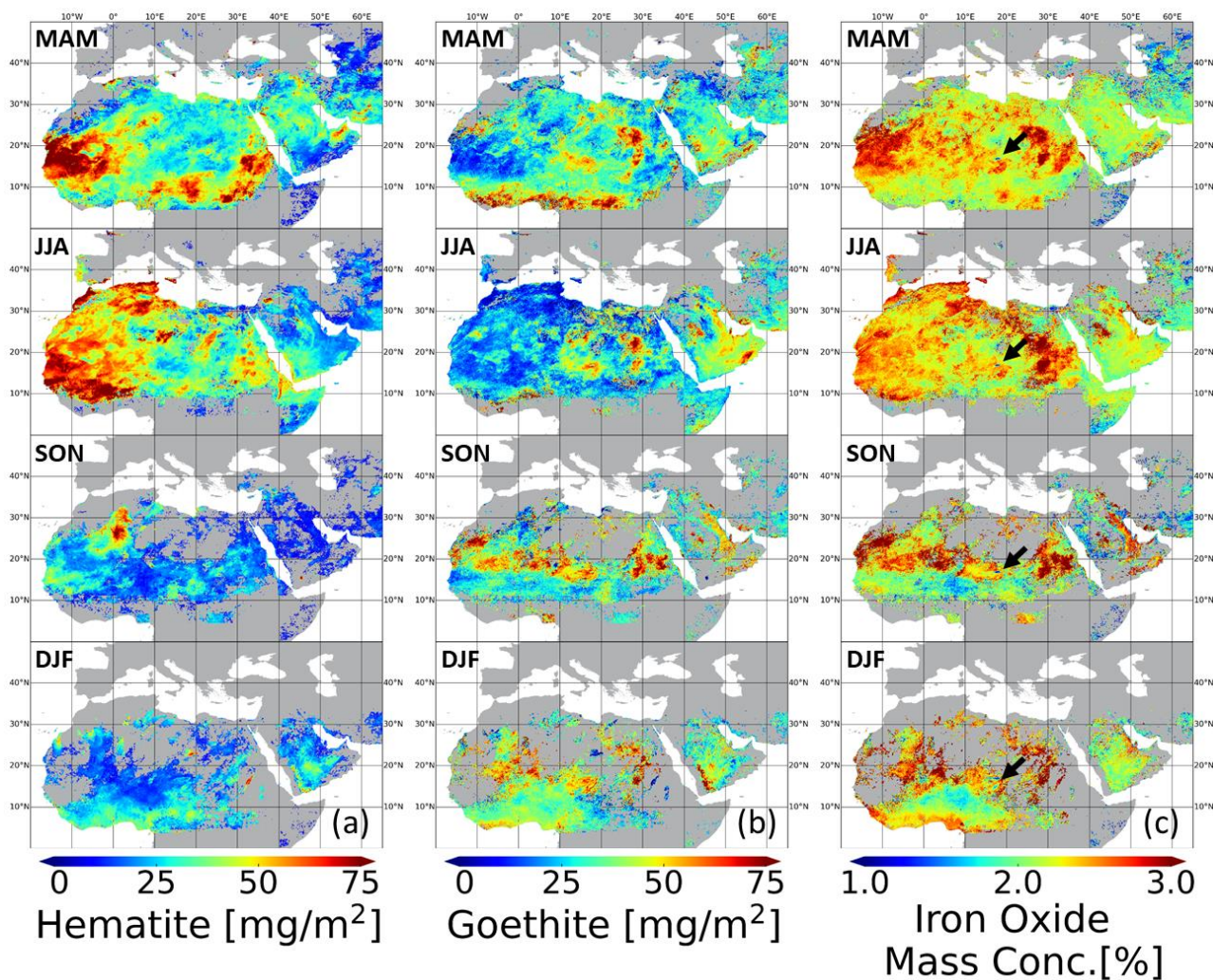
Globally, our iron-oxide mass concentrations were in the range of up to ~6.5 wt.%, consistent with the generally accepted
range (Di Biagio et al., 2019; Schuster et al., 2016).

The North Africa and Middle East (Fig. 9) areas exhibit increasing AOD throughout by spring and summer (barring the
595 rainy season over the Sahel near Niger), with levels decreasing after autumn. Hematite, on the other hand, is likely prevalent
over Africa only during May–July, particularly over west Sahara near Mauritania where dust storms occur every year, often
transporting dust across the Atlantic Ocean to Puerto Rico and northern Brazil. Our visual analysis implies that these high dust
hematite concentrations (especially in May) are due to transport from central Algeria, Mali, and sometimes the Sudan, with
transport westward across the Sahel line. Otherwise, goethite was more prevalent than hematite over the Sahara and Sahel
600 (Formenti et al., 2014a).

The Bodélé Depression area has lower iron-oxide concentration of close to ~1 wt.% with high AOD throughout the year
(Todd et al. 2007; Moskowitz et al., 2016). Higher iron-oxide concentrations are also well documented for the Sahelian area
(0°–20° N) and in the Sahara, particularly in April (not shown). Sahel dust is richer in iron-oxide than Saharan and Chinese
dust, as found by Clauquin et al. (1999) and Lafon et al. (2004).

605 Over Asia (Fig. 10), Taklimakan dust contained twice as much goethite as hematite during March–October (Shen et al.,
2006). The Gobi Desert showed widespread dust activity overall with higher goethite concentrations during March–May, with
less in summer. India had higher hematite concentrations during the pre-monsoon season, especially in May.

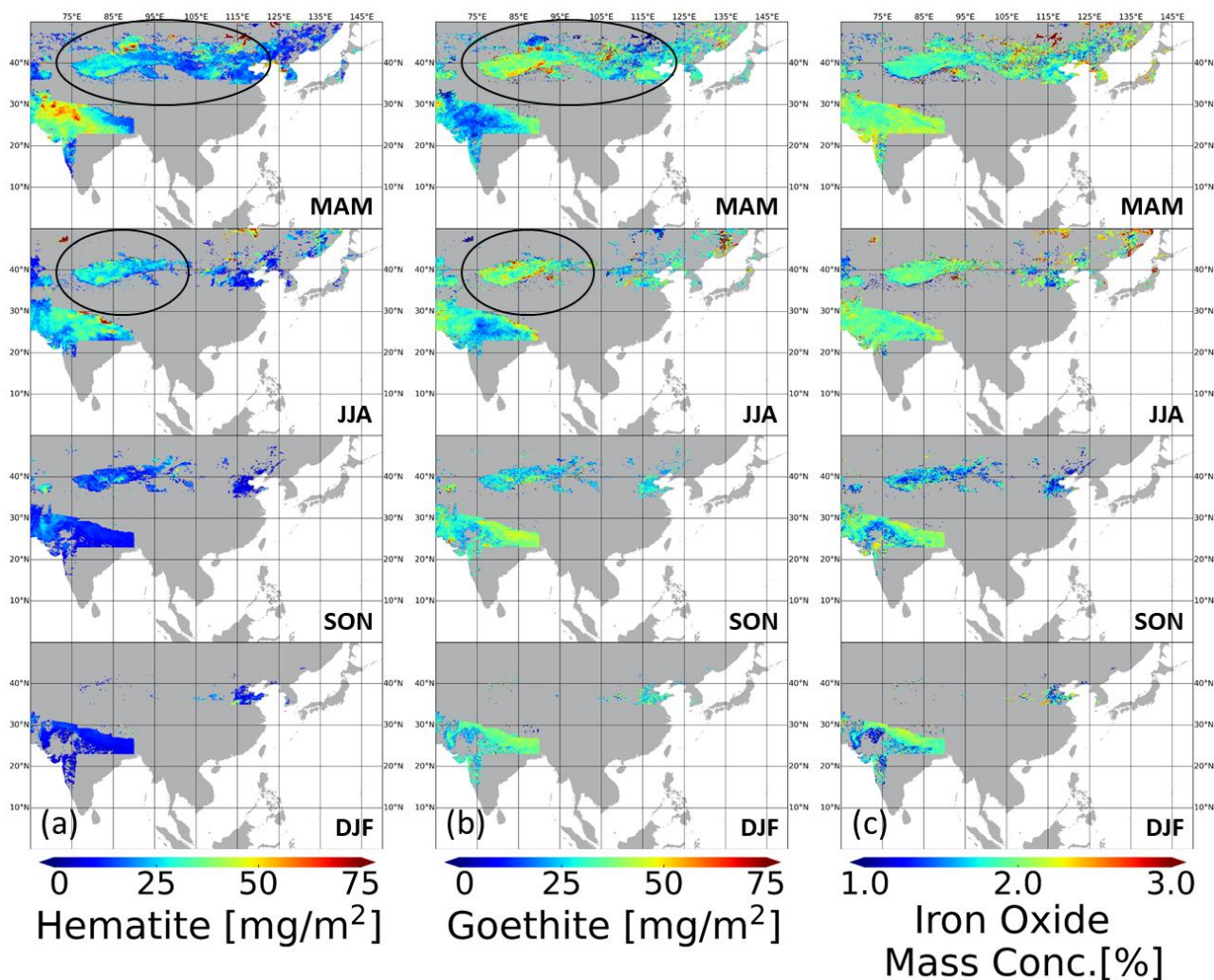
Other well-known dust areas, which have not been extensively used as case studies, occur east of the Aral Sea, in the
southeastern coastal region of the Caspian Sea, in eastern Uzbekistan and Turkmenistan, and in the southwestern corner of
610 Afghanistan, all of which are known highly active dust sources (Ginoux et al., 2012), but knowledge of their dust mineral
composition is lacking.



615

620

Figure 9: Seasonally average data for Sahara–Sahel and Middle East dust source areas generated from MAIAC EPIC 2018 data, (January 1 to December 31): (a) hematite mass concentration (mg m^{-2}); (b) goethite mass concentration (mg m^{-2}); (c) iron-oxide mass concentration (wt.%), with one row per season (row 1, March, April, and May (MAM); row 2, June, July, and August (JJA); row 3, September, October, and November (SON); row 4, December, January, and February (DJF)). Climatology data may include some mixed aerosol and smoke aerosol cases causing bias relative to pure dust cases (Fig. 5; Figs A1–A6). Four black arrows over (c) are pointing at the Bodélé Depression area. Additional data for AOD at 443 nm, SSA at 443 nm, and total number of datapoints used in this figure are provided in Fig. S2.



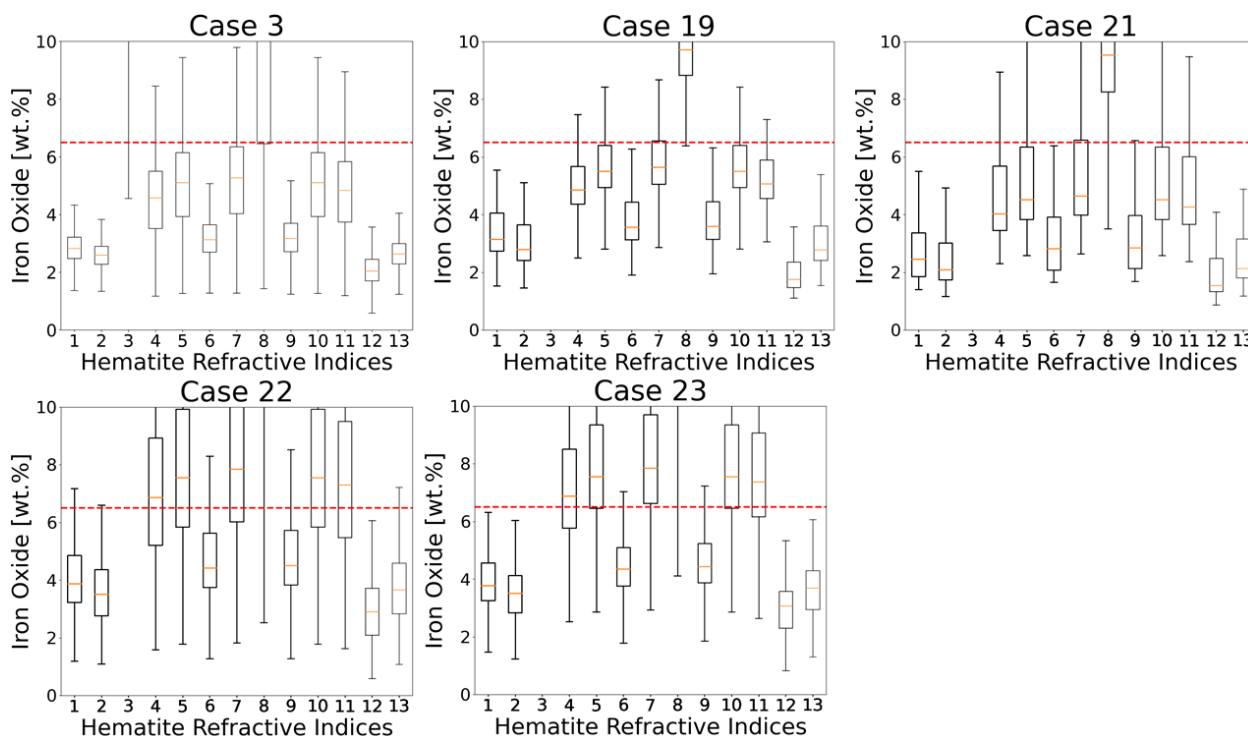
625 **Figure 10:** The same as in Fig. 9 but for Asia. Additional data of AOD at 443 nm, SSA at 443 nm, and total number of datapoints used in this figure are provided in Fig. S3.

4 Implication from different hematite refractive indices

630 Hematite refractive indices exhibit a large range in the literature, as introduced in section 2.3 and Fig. 3. This is critical since the retrieved hematite and goethite content vary significantly depending on the *a priori* refractive index of hematite. To find the most suitable *a priori* hematite refractive index, we analyzed how much the hematite and goethite content change



quantitatively with respect to our *a priori* hematite refractive index for the 24 dust cases presented in section 3.1. Note that, some of the literatures do not include real refractive indices, such as Gillespie and Lindberg (1992), Marusak et al. (1980), and
635 Vernon (1962), so we used the Scanza et al. (2015) real refractive index of hematite as an alternative.



640 **Figure 11:** Box and whisker plot of iron-oxide content by mass (wt.%; y axis) for 13 models of hematite refractive index (x axis; number 1–13, see Table 1) for the dust cases 3, 19, 21, 22, and 23 presented in section 3.1. Red horizontal dashed line on each figure shows the maximum expected iron-oxide content (6.5 wt.%) based on *in situ* measurements.

Fig. 11 depicts the box and whisker plot of iron-oxide content by mass (wt.%) with respect to 13 kinds of *a priori* hematite refractive indices (Fig. 3; Table 1) for the selected 5 dust cases (case 3, 19, 21, 22, 23; for all 24 dust cases, see Fig. S6). Note that the goethite density vary in the literature ($\rho_{goethite} = 3800 \text{ kg m}^{-3}$ of Bedidi and Cervelle (1993); $\rho_{goethite} = 4280 \text{ kg m}^{-3}$
645 of Formenti et al. (2014a)), but does not affect the calculated iron-oxide content (wt.%) significantly, as the retrieved volume fraction of goethite mostly small (less than 0.03) as opposed to over 0.9 volume fraction of host (not shown).

In literature, the *in situ* measurement of maximum of iron-oxide content is about 6.5 wt.% (2–5 wt.% of Linke et al. (2006) and Formenti et al. (2014b)); 2.8–5 wt.% of Lafon et al. (2004); 2.4–4.5 wt.% of Formenti et al. (2008); 0.7–5.8 wt.% of Di Biagio et al. (2019); 2.8–6.5 wt.% of Lafon et al. (2006)). This indicates that the hematite refractive indices of ‘3. Krekov
650 (1992)’ and ‘8. Bedidi and Cervelle (1993)’ are not viable for our approach, since the corresponding retrieved iron-oxide contents mostly exceed 6.5 wt.%. Specifically, the lower quartile for ‘3. Krekov (1992)’ is always over 10 wt.%, therefore not



visible in Fig. 11 (also not visible in Fig. S6). The lower quartile for ‘8. Bedidi and Cervelle (1993)’ exceed 6.5 wt.% in 11 cases among 24 dust cases (case 3, 4, 5, 6, 7, 13, 18, 19, 21, 22, 23).

Based on the same logic, hematite refractive index of ‘4. Gillespie and Lindberg (1992)’, ‘5. Hsu and Matijevic (1985)’, ‘7. Longtin et al. (1988)’, ‘10. Kerker et al. (1979)’, and ‘11. Marusak et al. (1980)’ do not produce reasonable results. For example, in dust case 22 and 23 over Australia, the median values of iron-oxide content already exceed 6.5 wt.%. In case 3, 19, 21, the upper quartile of the iron-oxide content is close to 6.5 wt.%.

We exclude ‘9. Sokolik and Toon (1999)’ from the most suitable hematite refractive index. ‘9. Sokolik and Toon (1999)’ cited Query (1978) for hematite, but Query (1978) measured complex refractive index of limestone, not hematite. It is suspected that ‘9. Sokolik and Toon (1999)’ misquoted ‘6. Query (1985)’ (Zhang et al., 2015), though there are slight differences between ‘9. Sokolik and Toon (1999)’ and ‘6. Query (1985)’.

Consequently, our analysis suggests that the remaining hematite refractive index of ‘1. Chen and Cahan (1981) –1’, ‘2. Chen and Cahan (1981) –2’, ‘6. Query (1985)’, ‘12. Vernon (1962)’, and ‘13. Scanza et al., (2015)’ are the most plausible (summarized in Fig. S7). These results are in agreement with Schuster et al. (2016) selecting Chen and Cahan (1981) as the baseline refractive index of hematite. Li et al. (2019) paper used both Scanza et al. (2015) and Longtin et al. (1988) as a representative of iron oxides, mentioned the large range of hematite refractive indices, but did not search for the most plausible one.

It is worth to mention that we cannot narrow down the most plausible hematite refractive index with the corresponding cost function only. This is because we fit the exponentially decreasing imaginary refractive index of MAIAC EPIC with wavelength at 340, 388, 443, and 680 nm derived from equation (10) parametrized only with b and k_0 . Some of the hematite refractive indices, such as ‘5. Hsu and Matijevic (1985)’, ‘7. Longtin et al. (1988)’, and ‘10. Kerker et al. (1979)’, have exponentially decreasing imaginary refractive index at 350–400 nm, therefore the minimum cost function is always less than 0.003 (in Fig. S10). On the contrary, hematite refractive indices, such as ‘1. Chen and Cahan (1981) –1’, ‘2. Chen and Cahan (1981) –2’, ‘6. Query (1985)’, ‘9. Sokolik and Toon (1999)’, and ‘13. Scanza et al. (2015)’ (used in this study), have increasing imaginary refractive index at 350–400 nm, therefore the magnitude of cost function (Fig. S10) is proportional to hematite volume fraction (Fig. S8).

5 Conclusions

In our knowledge, this is the first attempt to infer hematite and goethite concentrations, primary components of iron oxides, from the single-viewing satellite measurements. Based on the rationale that hematite and goethite are the major components causing absorption in the UV–Vis region, we used the Maxwell–Garnett effective medium approximation method with the



685 EPIC spectral aerosol absorption information k_0 and b . Currently, this algorithm uses pure-dust cases and may be biased in regions/seasons where dust aerosol is mixed with biomass burning smoke. Our retrieval patterns were generally consistent in time and space with those of previous studies over main global dust source areas.

Sites in the central Sahara and Sahel, such as Libya, Algeria, Mauritania, Niger, Mali, and Bodélé, and in the Middle East such as Saudi Arabia and Kuwait, exhibit greater temporal variability than other sites, implying large dynamic dust-source variability in the Sahara, Sahel, and Middle East. Over the central Sahara and Sahel regions, goethite was generally prevalent except for during the summer monsoon season of May–July, when hematite was predominant and likely sourced from near 690 Algeria, Mali, and Sudan. The Bodélé Depression area has distinctive lower iron-oxide concentration on climatology map (~1 wt.%) with high AOD throughout the year. Over the Middle East, goethite was prevalent in the Shamal season, whereas hematite was widespread in the atmosphere during March–May. Over India, higher hematite concentrations were detected in 2018 during the pre-monsoon season. The Taklimakan Desert was active except for in winter, with hematite/goethite ratios of ~0.55 (near published values). The Gobi Desert also had a ratio of 0.55 but was active only during spring. Over North America 695 and Australia, pure-dust-episode analysis indicated hematite-dominated patterns, consistent with earlier studies. Our results, including the 24 representative dust cases over different continental area, clearly implied that the composition of hematite to goethite may differ case by case depending on different source regions, meteorological condition causing transportation, even within a day.

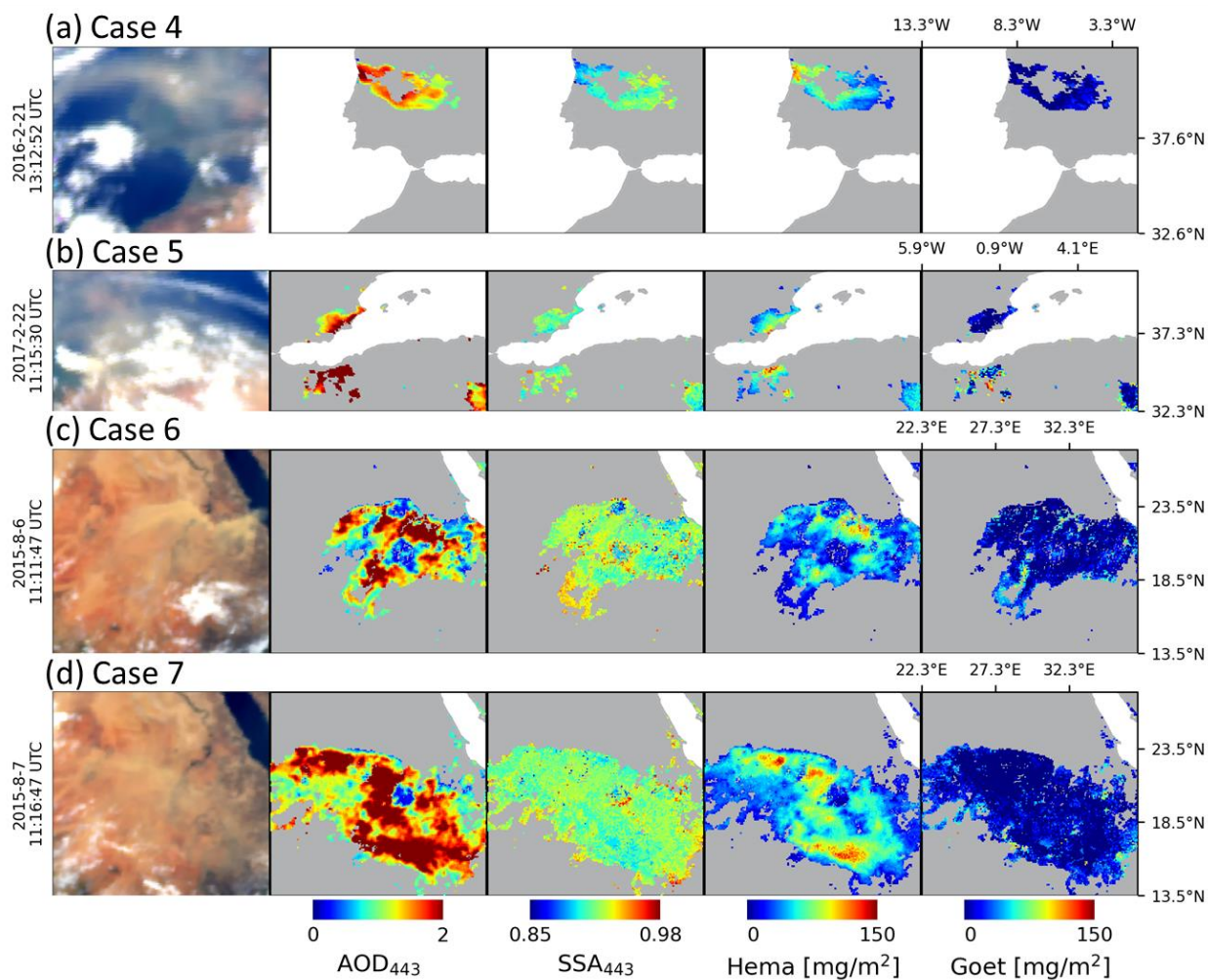
We compared our retrieval data with the Di Biagio et al. (2019) who undertook only soil analyses. While our retrievals 700 may include both local and long-range-transport contributions of iron oxides; our results cover the range of soil data both qualitatively (relative comparisons site by site) and quantitatively. This implies that our retrieval data are robust. There seemed to be better agreement during seasons of local erosion without long-range transport. Further quantitative comparisons are needed with widespread ground-based data such as AERONET, if it becomes available.

We also selected the most plausible hematite refractive indices, given that the maximum value of iron-oxide content that 705 we have found with *in situ* measurement papers is about 6.5 wt.%. The narrowed-down hematite refractive indices, such as Chen and Cahan (1981), Querry (1985), Vernon (1962), and Scanza et al. (2015), exhibited a similar range and spectral shape, and are in agreement with Schuster et al. (2016).

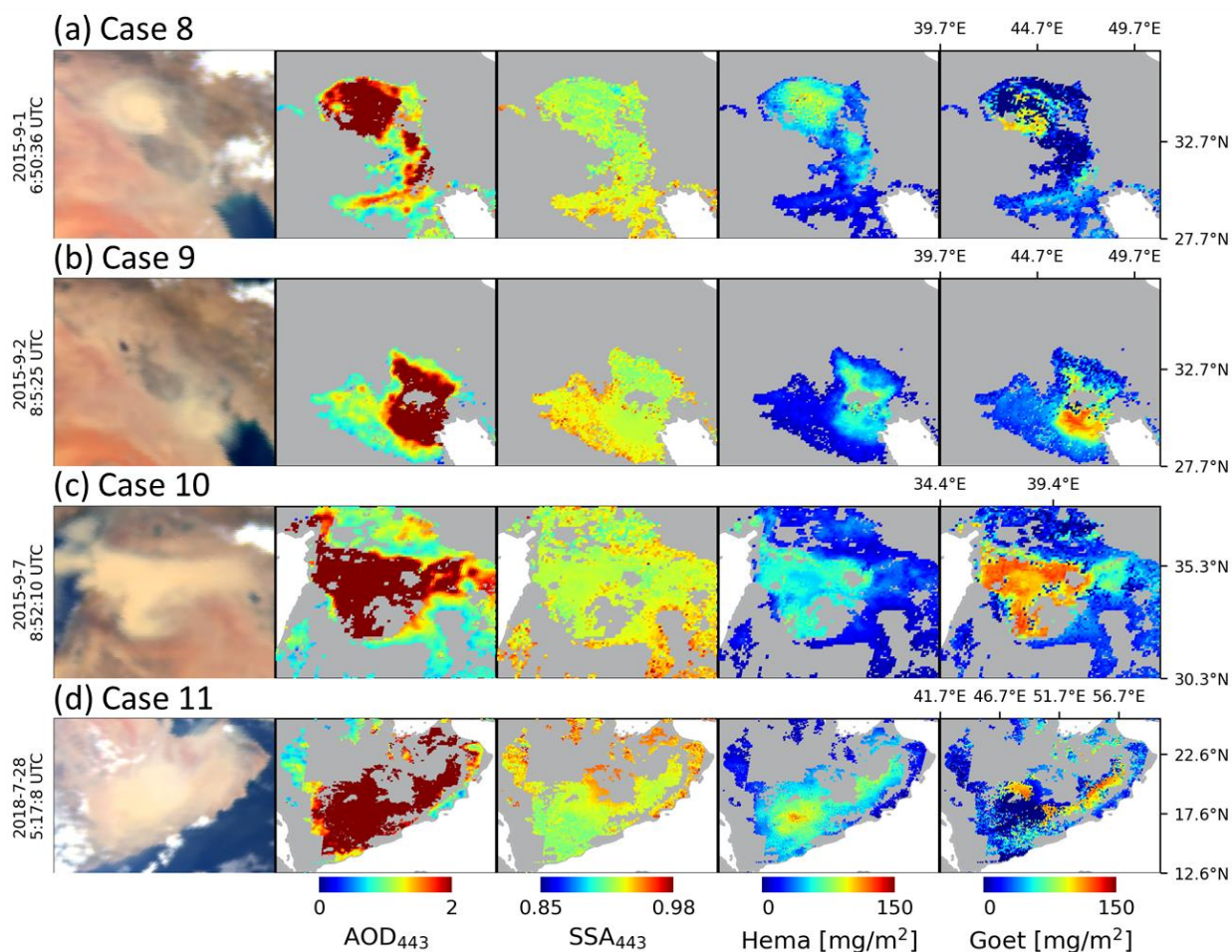
The developed algorithm can be applied for other on-orbit instruments with UV–Vis channels. The reported results from EPIC for the first time provide the global over land climatology of hematite and goethite concentrations in mineral dust, and 710 should be useful for the estimation of SW dust DRE in Earth-system and climate modeling.



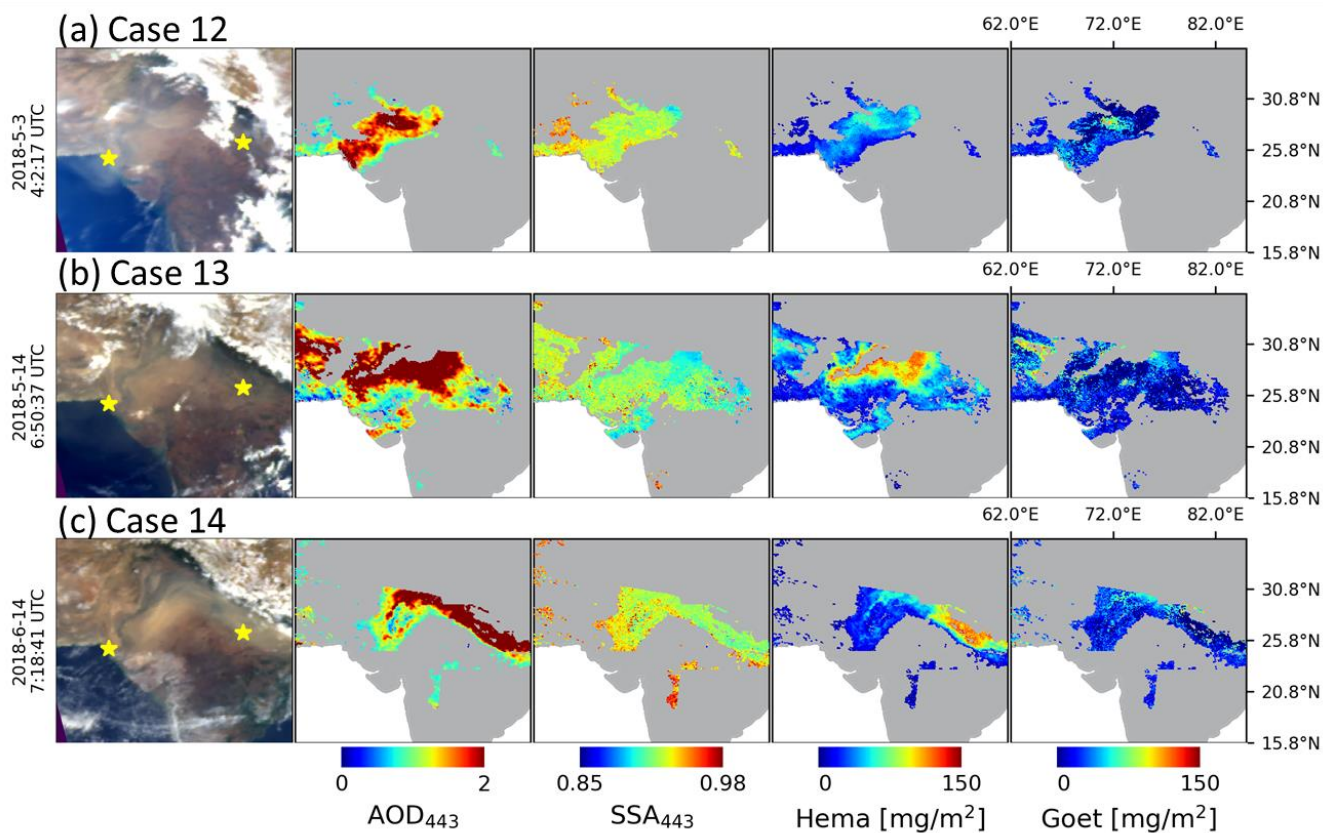
Appendix A



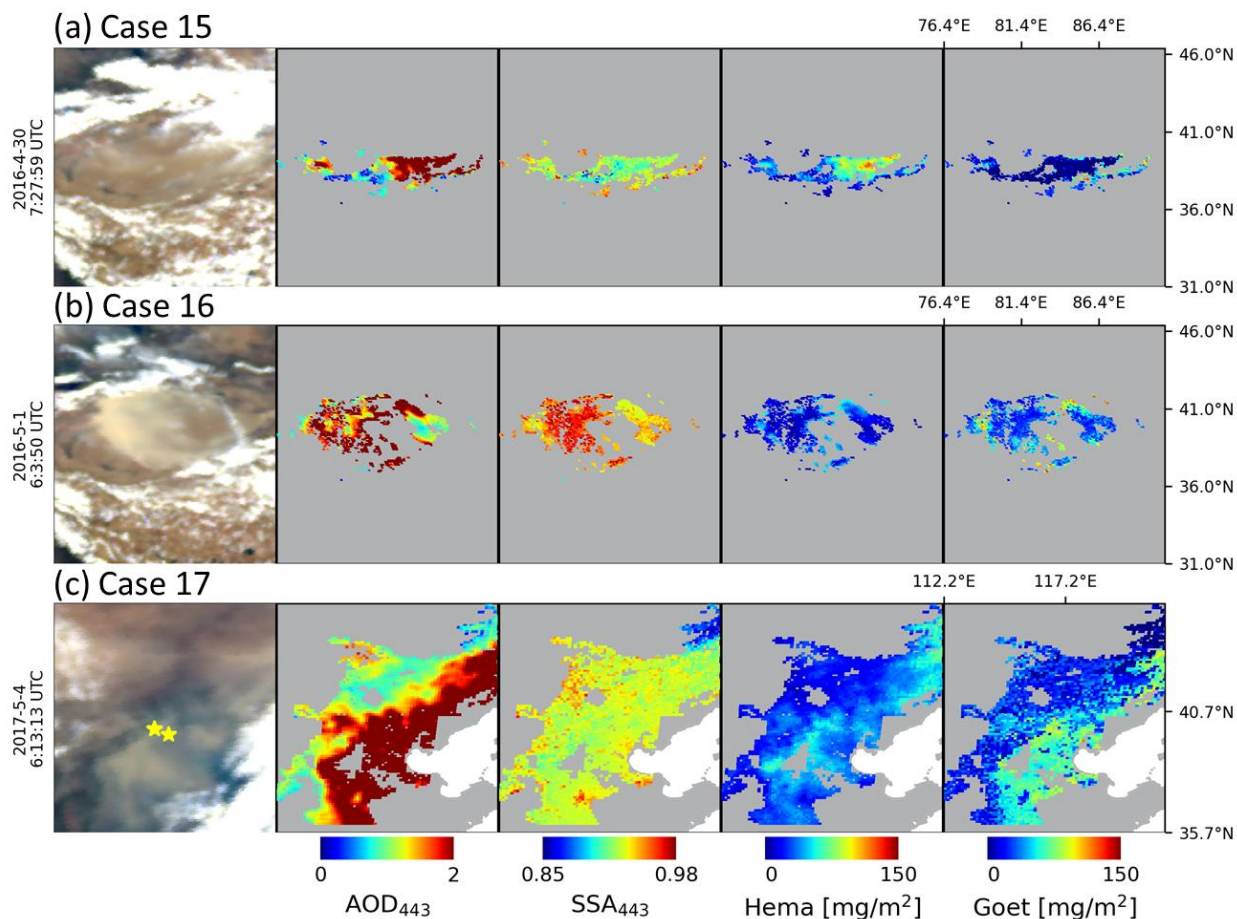
715 **Figure A1:** Dust episodes over the northern Sahara (rows 1 and 2) and near the Red Sea (rows 3 and 4). From left, RGB TOA image generated from EPIC L1B version 3 data, AOD and SSA at 443 nm, mass concentration of hematite and goethite for each case: Case 4 (row 1), dust episode on February 21, 2016; Case 5 (row 2), dust episode on February 22, 2017; Case 6 (row 3), dust episodes on August 6, 2015; Case 7 (row 4), dust episodes on August 7, 2015.



720 **Figure A2: Dust episodes over the Middle East. From left, RGB TOA image generated from EPIC L1B version 3 data, AOD 443 nm, SSA 443 nm, hematite mass concentration, and goethite mass concentration for each case: Case 8 (row 1), dust episode on September 1, 2015; Case 9 (row 2), dust episode on September 2, 2015; Case 10 (row 3), dust episodes on September 7, 2015; Case 11 (row 4) dust episode on July 28, 2018.**



725 **Figure A3: Dust episodes over India. From left, RGB TOA image generated from EPIC L1B version 3 data, AOD 443 nm, SSA 443 nm, hematite mass concentration, and goethite mass concentration for each case: Case 12 (row 1), dust episode on May 3, 2018; Case 13 (row 2), dust episode on May 14, 2018; Case 14 (row 3), dust episode on June 14, 2018. Yellow stars indicate AERONET sites at Karachi (24.946°N, 67.136°E) and Kanpur (26.513°N, 80.232°E).**



730

Figure A4: Dust episodes over the Taklimakan (rows 1 and 2) and Gobi (row 3) deserts. From left, RGB TOA image generated from EPIC L1B version 3 data, AOD 443 nm, SSA 443 nm, hematite mass concentration, and goethite mass concentration for each case: Case 15 (row 1), dust episode on April 30, 2016; Case 16 (row 2), dust episode on May 1, 2016; Case 17 (row 3) dust episode on May 4, 2017. Yellow stars over Case 17 (row 3) indicate AERONET sites at Beijing (39.977°N, 116.381°E), Beijing_RADI (40.005°N, 116.379°E), and XiangHe (39.754°N, 116.962°E).

735

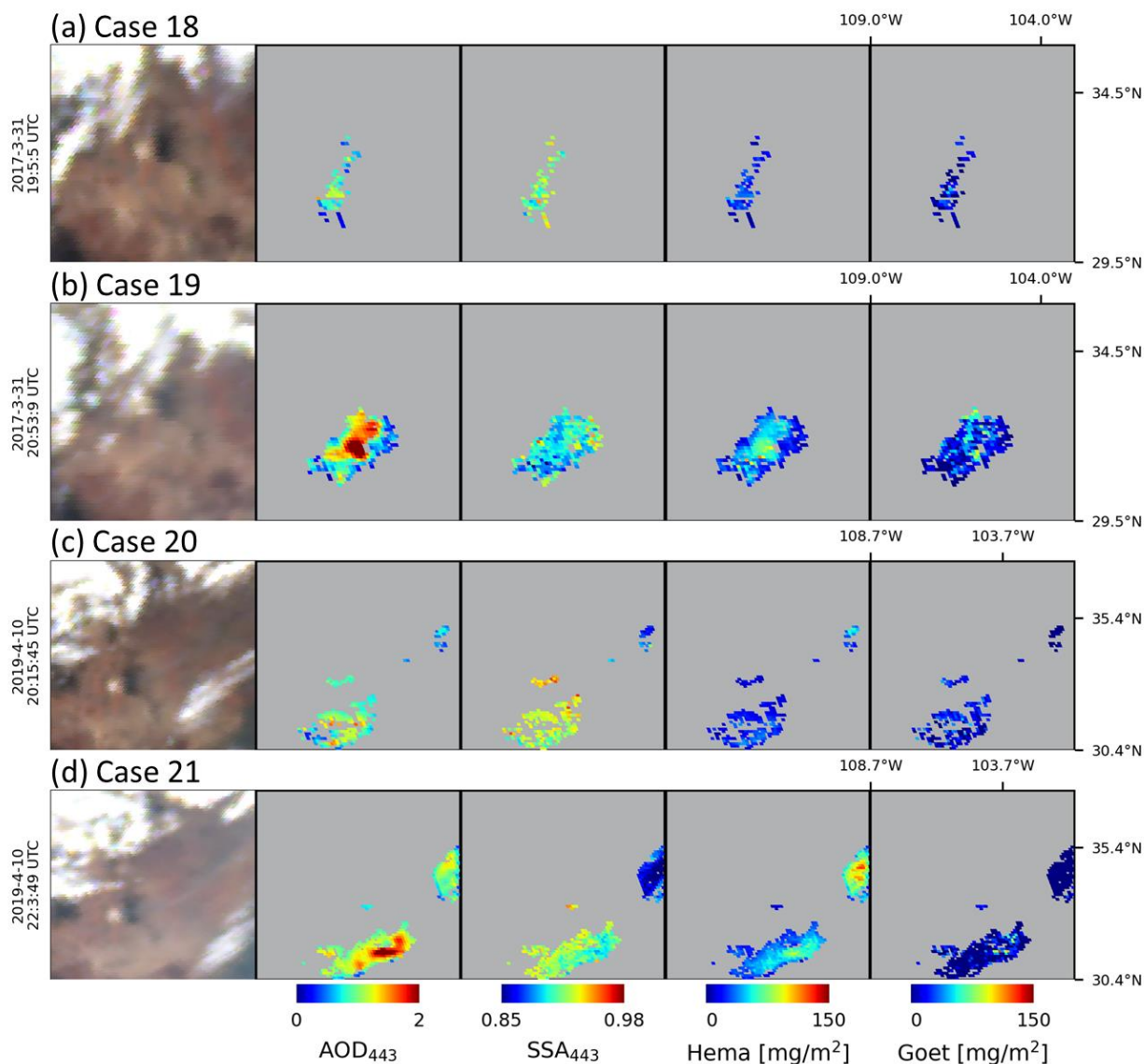
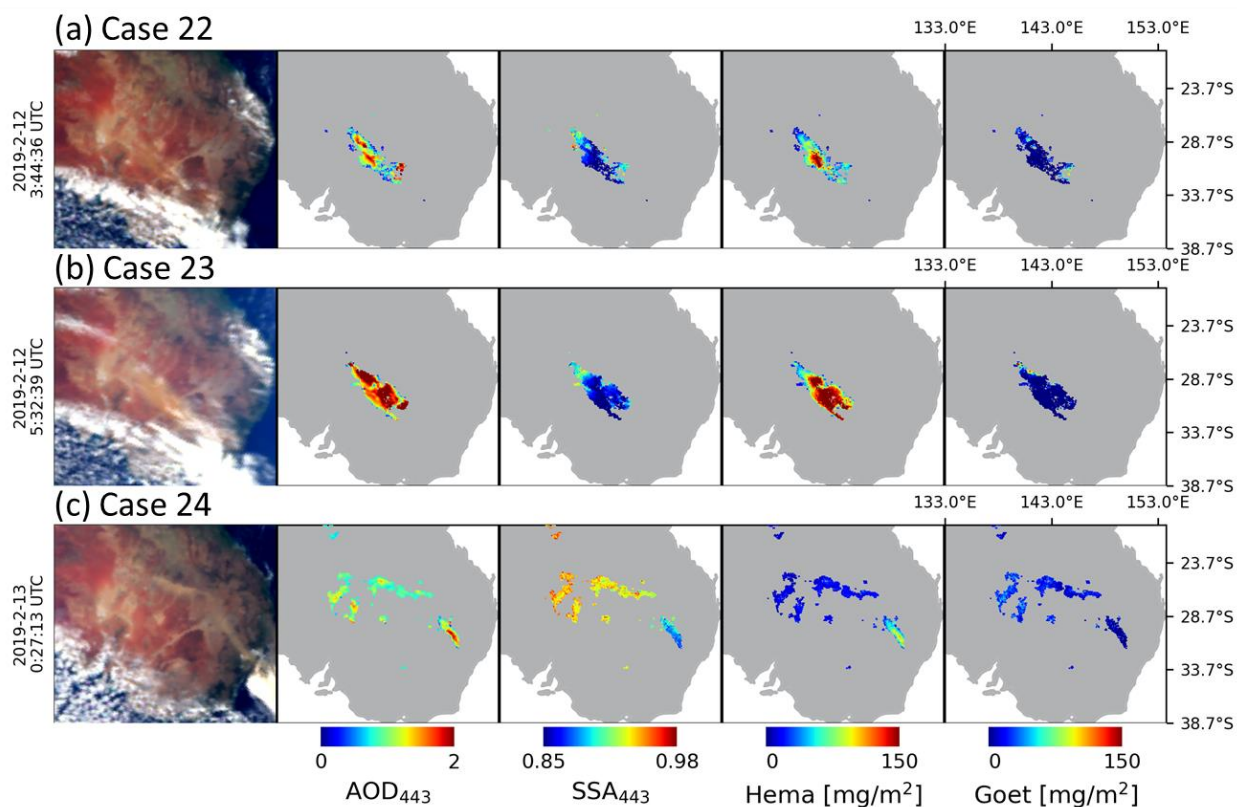


Figure A5: Dust episodes over North America near New Mexico, USA. From left, RGB TOA image generated from EPIC L1B version 3 data, AOD 443 nm, SSA 443 nm, hematite mass concentration, and goethite mass concentration for each case: Case 18 (row 1), dust episode on March 31, 2017, 19:00 UTC; Case 19 (row 2), dust episode on March 31, 2017, 20:00 UTC; Case 20 (row 3), dust episode on April 10, 2019, 20:00 UTC; Case 21 (row 4), dust episode on April 10, 2019, 22:00 UTC.

740



745 **Figure A6: Dust episodes over Australia.** From left, RGB TOA image generated from EPIC L1B version 3 data, AOD 443 nm, SSA 443 nm, hematite mass concentration, and goethite mass concentration for each case: Case 22 (row 1), dust episode on February 12, 2019, 03:00 UTC; Case 23 (row 2), dust episode on February 12, 2019, 05:00 UTC; Case 24 (row 3), dust episodes on February 13, 2019.



Author contributions.

750 SG and AL designed the study with discussions with GLS and MC. GLS provided major guidance on the algorithm development and data analysis. AL provided the MAIAC EPIC products. OK participated in the collection of hematite refractive indices data. SG, AL, and MC developed the code and performed the retrievals. SG, AL, GLS, and MC analyzed results. SG and AL wrote the manuscript with comments from GLS, MC, PG, MC, OK, OD, JK, ADS, BH, and JSR.

755 Competing interests.

The authors declare that they have no conflict of interest.

Acknowledgements.

760 The work of A. Lyapustin, S. Go, and M. Choi was funded by the NASA DSCOVR program (manager Dr. R. Eckman) and in part by the NASA PACE program (19-PACESAT19-0039). We are grateful to the AERONET team for providing validation data and to the NASA Center for Climate Simulations providing resources for the EPIC data processing. Co-author J. S Reid was supported by the Office of Naval Research Code 322.



References

- 765 Arimoto, R., Balsam, W., and Schloesslin, C.: Visible spectroscopy of aerosol particles collected on filters: iron-oxide minerals, *Atmos. Environ.*, 36, 89–96, 2002.
- Arola, A., Schuster, G., Myhre, G., Kazadzis, S., Dey, S., and Tripathi, S. N.: Inferring absorbing organic carbon content from AERONET data, *Atmos. Chem. Phys.*, 11, 215–225, <https://doi.org/10.5194/acp-11-215-2011>, 2011.
- Balkanski, Y., Schulz, M., Claquin, T., and Guibert, S.: Reevaluation of Mineral aerosol radiative forcings suggests a better
770 agreement with satellite and AERONET data, *Atmos. Chem. Phys.*, 7, 81–95, <https://doi.org/10.5194/acp-7-81-2007>, 2007.
- Bedidi, A. and Cervelle, B.: Light scattering by spherical particles with hematite and goethite like optical properties: Effect of water impregnation, *J. Geophys. Res.*, 98, 11941–11952, 1993.
- Bohren, C. and Huffman, D.: *Absorption and Scattering of Light by Small Particles*, Wiley, New York, NY, USA, 1983.
- 775 Boucher, O., Randall, D., Artaxo, P., Bretherton, C., Feingold, G., Forster, P., Kerminen, V.-M., Kondo, Y., Liao, H., Lohman, U., Rasch, P., Satheesh, S., Sherwood, S., Stevens, B., Zhang, X.-Y., Lohmann, U., Rasch, P., Satheesh, S., Sherwood, S., Stevens, B., and Zhang, X.-Y.: Clouds and Aerosols, in: *Climate Change 2013: The Physical Science Basis*, Contribution of Working Group I to the Fifth Assessment Report of the Intergovernmental Panel on Climate Change, edited by: Stocker, V. B., Qin, T. F. D., Plattner, G.-K., Tignor, M., Allen, S. K., Boschung, J., Nauels, A.,
780 Xia, Y., and Midgley, P. M., Cambridge University Press, Cambridge, United Kingdom, 573–657, 2013.
- Chen, C. T. and Cahan, B. D.: Visible and ultraviolet optical properties of single-crystal and polycrystalline hematite measured by spectroscopic ellipsometry, *J. Opt. Soc. Am.*, 71, 932–934, 1981.
- Claquin, T., Schulz, M., and Balkanski, Y.: Modeling the mineralogy of atmospheric dust sources, *J. Geophys. Res.*, 104, 22222–243256, 1999.
- 785 Di Biagio, C., Formenti, P., Balkanski, Y., Caponi, L., Cazaunau, M., Pangui, E., Journet, E., Nowak, S., Caquineau, S., Andreae, M. O., Kandler, K., Saeed, T., Piketh, S., Seibert, D., Williams, E., and Doussin, J.-F.: Global scale variability of the mineral dust long-wave refractive index: a new dataset of in situ measurements for climate modeling and remote sensing, *Atmos. Chem. Phys.*, 17, 1901–1929, <https://doi.org/10.5194/acp17-1901-2017>, 2017.
- Di Biagio, C., Formenti, P., Balkanski, Y., Caponi, L., Cazaunau, M., Pangui, E., Journet, E., Nowak, S., Andreae, M. O.,
790 Kandler, K., Saeed, T., Piketh, S., Seibert, D., Williams, E., and Doussin, J.-F.: Complex refractive indices and single-scattering albedo of global dust aerosols in the shortwave spectrum and relationship to size and iron content, *Atmos. Chem. Phys.*, 19, 15503–15531, <https://doi.org/10.5194/acp-19-15503-2019>, 2019.
- Di Biagio, C., Balkanski, Y., Albani, S., Boucher, O., and Formenti, P.: Direct Radiative Effect by Mineral Dust Aerosols Constrained by New Microphysical and Spectral Optical Data, *Geophys. Res. Lett.*, 47, 1–12,
795 <https://doi.org/10.1029/2019GL086186>, 2020.



- Diner, D. J., Boland, S. W., Brauer, M., Bruegge, C., Burke, K. A., Chipman, R., Di Girolamo, L., Garay, M. J., Hasheminassab, S., Hyer, E., Jerrett, M., Jovanovic, V., Kalashnikova, O. V., Liu, Y., Lyapustin, A. I., Martin, R. V., Nastan, A., Ostro, B. D., Ritz, B., Schwartz, J., Wang, J., and Xu, F.: Advances in multiangle satellite remote sensing of speciated airborne particulate matter and association with adverse health effects: from MISR to MAIA, *J. Appl. Remote Sens.*, 12, 042603, <https://doi.org/10.1117/1.JRS.12.042603>, 2018.
- 800 Dubovik, O., Holben, B., Eck, T. F., Smirnov, A., Kaufmann, Y. J., King, M. D., Tanré, D., and Slutsker, I.: Variability of absorption and optical properties of key aerosol types observed in worldwide locations, *J. Atmos. Sci.*, 59, 590–608, [https://doi.org/10.1175/1520-0469\(2002\)0592.0.CO;2](https://doi.org/10.1175/1520-0469(2002)0592.0.CO;2), 2002.
- Eck, T. F., Holben, B. N., Sinyuk, A., Pinker, R. T., Goloub, P., Chen, H., Chatenet, B., Li, Z., Singh, R. P., Tripathi, S. N., 805 Reid, J. S., Giles, D. M., Dubovik, O., O'Neill, N. T., Smirnov, A., Wang, P., and Xia, X.: Climatological aspects of the optical properties of fine/coarse mode aerosol mixtures, *J. Geophys. Res.*, 115, doi:10.1029/2010JD014002, 2010
- Fitzpatrick, R. W.: Changes in soil and water characteristics of natural, drained and reflooded soils in the Mesopotamian marshlands: Implications for land management planning. CSIRO land and water: client report, 2004.
- Formenti, P., Rajot, J. L., Desboeufs, K., Caquineau, S., Chevaillier, S., Nava, S., Gaudichet, A., Journet, E., Triquet, S., and 810 Alfaro, S.: Regional variability of the composition of mineral dust from western Africa: results from the AMMA SOP0/DABEX and DODO field campaigns, *J. Geophys. Res.-Atmos.*, 113, D00C13, doi:10.1029/2008JD009903, 2008.
- Formenti, P., Caquineau, S., Chevaillier, S., Klaver, A., Desboeufs, K., Rajot, J. L., Belin, S., and Briois, V.: Dominance of goethite over hematite in iron oxides of mineral dust from Western Africa: Quantitative partitioning by X-ray 815 absorption spectroscopy, *J. Geophys. Res.-Atmos.*, 119, 12740–12754, <https://doi.org/10.1002/2014JD021668>, 2014a.
- Formenti, P., Caquineau, S., Desboeufs, K., Klaver, A., Chevaillier, S., Journet, E., and Rajot, J. L.: Mapping the physicochemical properties of mineral dust in western Africa: mineralogical composition, *Atmos. Chem. Phys.*, 14, 10663–10686, doi:10.5194/acp-14-10663-2014, 2014b.
- 820 Formenti, P., Schütz, L., Balkanski, Y., Desboeufs, K., Ebert, M., Kandler, K., Petzold, A., Scheuven, D., Weinbruch, S., and Zhang, D.: Recent progress in understanding physical and chemical properties of African and Asian mineral dust, *Atmos. Chem. Phys.*, 11, 8231–8256, doi:10.5194/acp-11-8231-2011, 2011a.
- Formenti, P., Rajot, J. L., Desboeufs, K., Saïd, F., Grand, N., Chevaillier, S., and Schmechtig, C.: Airborne observations of mineral dust over western Africa in the summer Monsoon season: spatial and vertical variability of physico-chemical 825 and optical properties, *Atmos. Chem. Phys.*, 11, 6387–6410, doi:10.5194/acp-11-6387-2011, 2011b.
- Galuzza, A., Eremenko, V., and Kirichenko, A.: Analysis of hematite reflection spectrum by the Kramers-Kronig method, *Sov. Phys. Sol. State*, 21, 654–656, 1979.



- Gillespie, J. B. and Lindberg, J. D.: Ultraviolet and visible imaginary refractive index of strongly absorbing atmospheric particulate matter, *Appl. Optics*, 31, 2112–2115, 1992
- 830 Ginoux, P., Prospero, J., Gill, T. E., Hsu, N. C., and Zhao, M.: Global scale attribution of anthropogenic and natural dust sources and their emission rates based on MODIS deep blue aerosol products, *Rev. Geophys.*, 50, RG3005, <https://doi.org/10.1029/2012RG000388>, 2012.
- Glotch, T. D. and Rossman, G. R.: Mid-infrared reflectance spectra and optical constants of six iron oxide/oxyhydroxide phases, *Icarus*, 204, 663–671, 2009.
- 835 Green, R. O., Mahowald, N., Ung, C., Thompson, D. R., Bator, L., Bennet, M., Bernas, M., Blackway, N., Bradley, C., Cha, J., Clark, P., Clark, R., Cloud, D., Diaz, E., Ben Dor, E., Duren, R., Eastwood, M., Ehlmann, B. L., Fuentes, L., Ginoux, P., Gross, J., He, Y., Kalashnikova, O., Kert, W., Keymeulen, D., Klimesh, M., Ku, D., Kwong-Fu, H., Liggett, E., Li, L., Lundeen, S., Makowski, M. D., Mazer, A., Miller, R., Mouroulis, P., Oaida, B., Okin, G. S., Ortega, A., Oyake, A., Nguyen, H., Pace, T., Painter, T. H., Pempejian, J., Garcia-Pando, C. P., Pham, T., Phillips, B., Pollock, R., Purcell, R., Realmuto, V., Schoolcraft, J., Sen, A., Shin, S., Shaw, L., Soriano, M., Swayze, G., Thingvold, E., Vaid, A., and Zan, J.: The Earth Surface Mineral Dust Source Investigation: An Earth Science Imaging Spectroscopy Mission, in: 2020 IEEE Aerospace Conference, Big Sky, Montana, USA, 7–14 March 2020, 1–15, <https://doi.org/10.1109/AERO47225.2020.9172731>, 2020.
- 840 Hess, M., Kopke, P., and Schult, I.: Optical properties of aerosols and clouds: the software package OPAC, *B. Am. Meteorol. Soc.*, 79, 831–844, 1998.
- Hsu, W. P. and Matijevic, E.: Optical properties of monodispersed hematite hydrosols, *Appl. Optics*, 24, 1623–1630, 1985.
- Journet, E., Balkanski, Y., and Harrison, S. P.: A new data set of soil mineralogy for dust-cycle modeling, *Atmos. Chem. Phys.*, 14, 3801–3816, <https://doi.org/10.5194/acp-14-3801-2014>, 2014.
- Kalashnikova, O. V. and Sokolik, I. N.: Modeling the radiative properties of nonspherical soil-derived mineral aerosols, *J. Quant. Spectrosc. Ra.*, 87, 137–166, 2004.
- 850 Kerker, M., Scheiner, P., Cooke, D., and Kratochvil, J.: Absorption index and color of colloidal hematite, *J. Colloid Interf. Sci.*, 71, 176–187, 1979.
- Knippertz, P. and Stuut, J.-B. W. (Eds.): *Mineral Dust: A Key Player in the Earth System*, Springer Science & Business Media, Dordrecht, https://doi.org/10.1007/978-94-017-8978-3_1, 2014
- 855 Kok, J. F.: A scaling theory for the size distribution of emitted dust aerosols suggests climate models underestimate the size of the global dust cycle, *P. Natl. Acad. Sci. USA*, 108, 1016–1021, <https://doi.org/10.1073/pnas.1014798108>, 2011.
- Kok, J. F., Ridley, D. A., Zhou, Q., Miller, R. L., Zhao, C., Heald, C. L., Ward, D. S., Albani, S., and Haustein, K.: Smaller desert dust cooling effect estimated from analysis of dust size and abundance, *Nat. Geosci.*, 10, 274–278, <https://doi.org/10.1038/ngeo2912>, 2017.



- 860 Koven, C. D. and Fung, I.: Inferring dust composition from wavelength-dependent absorption in Aerosol Robotic Network (AERONET) data, *J. Geophys. Res.*, 111, D14205, <https://doi.org/10.1029/2005JD006678>, 2006.
- Krekov, G. M.: Models of atmospheric aerosols, in: *Aerosol Effects on Climate*, edited by: Jennings, S. G., Univ. of Ariz. Press, Tucson, 9–72, 1992.
- Lafon, S., Rajot, J., Alfaro, S., and Gaudichet, A.: Quantification of iron oxides in desert aerosol., *Atmos. Environ.*, 38, 1211–
865 1218, 2004.
- Lafon, S., Sokolik, I. N., Rajot, J. L., Caquineau, S., and Gaudichet, A.: Characterization of iron oxides in mineral dust aerosols: Implications for light absorption, *J. Geophys. Res.*, 111, D21207, <https://doi.org/10.1029/2005jd007016>, 2006.
- Lazaro, F. J., Gutierrez, L., Barrón, V., and Gelado, M. D.: The speciation of iron in desert dust collected in Gran Canaria (Canary Islands): Combined chemical, magnetic and optical analysis, *Atmos. Environ.*, 42, 8987–8996, 2008.
- 870 Li, L., Dubovik, O., Derimian, Y., Schuster, G. L., Lapyonok, T., Litvinov, P., Ducos, F., Fuertes, D., Chen, C., Li, Z., Lopatin, A., Torres, B., and Che, H.: Retrieval of aerosol components directly from satellite and ground-based measurements, *Atmos. Chem. Phys.*, 19, 13409–13443, <https://doi.org/10.5194/acp-19-13409-2019>, 2019.
- Li, L., Mahowald, N. M., Miller, R. L., Pérez García-Pando, C., Klose, M., Hamilton, D. S., Gonçalves Ageitos, M., Ginoux, P., Balkanski, Y., Green, R. O., Kalashnikova, O., Kok, J. F., Obiso, V., Paynter, D., and Thompson, D. R.:
875 Quantifying the range of the dust direct radiative effect due to source mineralogy uncertainty, *Atmos. Chem. Phys.*, 21, 3973–4005, <https://doi.org/10.5194/acp-21-3973-2021>, 2021.
- Li, Z., Gu, X., Wang, L., Li, D., Xie, Y., Li, K., Dubovik, O., Schuster, G., Goloub, P., Zhang, Y., Li, L., Ma, Y., and Xu, H.:
880 Aerosol physical and chemical properties retrieved from ground-based remote sensing measurements during heavy haze days in Beijing winter, *Atmos. Chem. Phys.*, 13, 10171–10183, <https://doi.org/10.5194/acp-13-10171-2013>, 2013.
- Li, Z., Li, L., Zhang, F., Li, D., Xie, Y., and Xu, H.: Comparison of aerosol properties over Beijing and Kanpur: Optical, physical properties and aerosol component composition retrieved from 12 years ground-based Sun-sky radiometer remote sensing data, *J. Geophys. Res.-Atmos.*, 120, 1520–1535, <https://doi.org/10.1002/2014JD022593>, 2015.
- 885 Linke, C., Möhler, O., Veres, A., Mohácsi, Á., Bozóki, Z., Szabó, G., and Schnaiter, M.: Optical properties and mineralogical composition of different Saharan mineral dust samples: a laboratory study, *Atmos. Chem. Phys.*, 6, 3315–3323, <https://doi.org/10.5194/acp-6-3315-2006>, 2006.
- Liu, X., Easter, R. C., Ghan, S. J., Zaveri, R., Rasch, P., Shi, X., Lamarque, J.-F., Gettelman, A., Morrison, H., Vitt, F., Conley, A., Park, S., Neale, R., Hannay, C., Ekman, A. M. L., Hess, P., Mahowald, N., Collins, W., Iacono, M. J., Bretherton, C. S., Flanner, M. G., and Mitchell, D.: Toward a minimal representation of aerosols in climate models: description
890 and evaluation in the Community Atmosphere Model CAM5, *Geosci. Model Dev.*, 5, 709–739, [doi:10.5194/gmd-5-709-2012](https://doi.org/10.5194/gmd-5-709-2012), 2012.



- Liu, X., Ma, P.-L., Wang, H., Tilmes, S., Singh, B., Easter, R. C., Ghan, S. J., and Rasch, P. J.: Description and evaluation of a new four-mode version of the Modal Aerosol Module (MAM4) within version 5.3 of the Community Atmosphere Model, *Geosci. Model Dev.*, 9, 505–522, <https://doi.org/10.5194/gmd-9-505-2016>, 2016.
- 895 Longtin, D. R., Shettle, E. P., Hummel, J. R., and Pryce, J. D.: A Wind Dependent Desert Aerosol Model: Radiative Properties, Air Force Geophys. Lab., Air Force Syst. Command Hanscom Air Force Base, Mass, AFGL-TR-88-0112, 115, 1988.
- Lyapustin, A., Go, S., Korkin, S., Wang, Y., Torres, O., Jethva, H. and Marshak, A.: Retrievals of Aerosol Optical Depth and Spectral Absorption from DSCOVR EPIC. *Front. Remote Sens.* 2:645794, doi: 10.3389/frsen.2021.645794, 2021.
- Lyapustin, A., Martonchik, J., Wang, Y., Laszlo, I., and Korkin, S.: Multi-Angle Implementation of Atmospheric Correction
900 (MAIAC): 1. Radiative Transfer Basis and Look-Up Tables, *J. Geophys. Res.*, 116, D03210, <https://doi.org/10.1029/2010JD014985>, 2011.
- Lyapustin, A., Wang, Y., Korkin, S., and Huang, D.: MODIS Collection 6 MAIAC algorithm, *Atmos. Meas. Tech.*, 11, 5741–5765, <https://doi.org/10.5194/amt-11-5741-2018>, 2018.
- Marusak, L. A., Messier, R., and White, W. B.: Optical absorption spectrum of hematite, $\alpha\text{Fe}_2\text{O}_3$ near IR to UV. *Journal of*
905 *Physics and Chemistry of Solids*, 41, 981-984, [https://doi.org/10.1016/0022-3697\(80\)90105-5](https://doi.org/10.1016/0022-3697(80)90105-5), 1980.
- Moosmüller, H., Engelbrecht, J. P., Skiba, M., Frey, G., Chakrabarty, R. K., and Arnott, W. P.: Single scattering albedo of fine mineral dust aerosols controlled by iron concentration, *J. Geophys. Res.*, 2006, 2004–2008, <https://doi.org/10.1029/2011JD016909>, 2012.
- Moskowitz, B. M., Reynolds, R. L., Goldstein, H. L., Berquó, T. S., Kokaly, R. F., and Bristow, C. S.: Iron oxide minerals in
910 dust-source sediments from the Bodélé Depression, Chad: Implications for radiative properties and Fe bioavailability of dust plumes from the Sahara, *Aeolian research*, 22, 93-106, <https://doi.org/10.1016/j.aeolia.2016.07.001>, 2016.
- Nicholson, S. E.: The ITCZ and the seasonal cycle over equatorial Africa. *Bulletin of the American Meteorological Society*, 99, 337-348, <https://doi.org/10.1175/BAMS-D-16-0287.1>, 2018.
- Onari, S., Arai, T., and Kudo, K.: Infrared lattice vibrations and dielectric dispersion in $\alpha\text{-Fe}_2\text{O}_3$, *Phys. Rev. B*, 16, 1717-1721,
915 1977.
- Perlwitz, J. P., Pérez García-Pando, C., and Miller, R. L.: Predicting the mineral composition of dust aerosols – Part 1: Representing key processes, *Atmos. Chem. Phys.*, 15, 11593–11627, <https://doi.org/10.5194/acp-15-11593-2015>, 2015a.
- Perlwitz, J. P., Pérez García-Pando, C., and Miller, R. L.: Predicting the mineral composition of dust aerosols – Part 2: Model
920 evaluation and identification of key processes with observations, *Atmos. Chem. Phys.*, 15, 11629–11652, <https://doi.org/10.5194/acp-15-11629-2015>, 2015b.
- Prospero, J. M., Ginoux, P., Torres, O., Nicholson, S. E., and Gill, T. E.: Environmental characterization of global sources of atmospheric soil dust identified with the Nimbus 7 Total Ozone Mapping Spectrometer (TOMS) absorbing aerosol product, *Rev. Geophys.*, 40, 1–31, 2002.



- 925 Query, M. R.: Optical Constants, Contractor report, US Army Chemical Research, Development and Engineering Center (CRDC), Aberdeen Proving Ground, MD, 418 pp., 1985.
- Query, M. R., Osborne, G., Lies, K., Jordon, R., and Coveney Jr., R. M.: Complex refractive index of limestone in the visible and infrared, *Appl. Optics*, 17, 353–356, 1978.
- Samset, B. H., Stjern, C. W., Andrews, E., Kahn, R. A., Myhre, G., Schulz, M., and Schuster, G. L.: Aerosol Absorption: Progress Towards Global and Regional Constraints, *Current Climate Change Reports*, 4, 65–83, <https://doi.org/10.1007/s40641-018-0091-4>, 2018.
- 930 Sarkar, S., Chauhan, A., Kumar, R., and Singh, R. P.: Impact of deadly dust storms (May 2018) on air quality, meteorological, and atmospheric parameters over the northern parts of India. *GeoHealth*, 3, 67–80, <https://doi.org/10.1029/2018GH000170>, 2019.
- 935 Scanza, R. A., Mahowald, N., Ghan, S., Zender, C. S., Kok, J. F., Liu, X., Zhang, Y., and Albani, S.: Modeling dust as component minerals in the Community Atmosphere Model: development of framework and impact on radiative forcing, *Atmos. Chem. Phys.*, 15, 537–561, <https://doi.org/10.5194/acp-15-537-2015>, 2015.
- Schuster, G. L., Dubovik, O., and Arola, A.: Remote sensing of soot carbon – Part 1: Distinguishing different absorbing aerosol species, *Atmos. Chem. Phys.*, 16, 1565–1585, <https://doi.org/10.5194/acp-16-1565-2016>, 2016.
- 940 Schuster, G. L., Dubovik, O., Holben, B. N., and Clothiaux, E. E.: Inferring black carbon content and specific absorption from Aerosol Robotic Network (AERONET) aerosol retrievals, *J. Geophys. Res.*, 110, D10S17, <https://doi.org/10.1029/2004JD004548>, 2005.
- Schwertmann, U.: Transformation of hematite to goethite in soils. *Nature*, 232, 624–625, <https://doi.org/10.1038/232624a0>, 1971.
- 945 Schwertmann, U.: Relations between iron oxides, soil color, and soil formation, in: Soil Science Society of America, edited by: Bigham, J. M. and Ciolkosz, E. J., *Soil Color*, Special Pub., Madison, WI, Vol. 31., 51–69, 1993.
- Shen, Z., Cao, J., Zhang, X., Arimoto, R., Ji, J., Balsam, W., Wang, Y., Zhang, R., and Li, X.: Spectroscopic analysis of iron-oxide minerals in aerosol particles from northern China, *Sci. Total Environ.*, 367, 899–907, 2006.
- Sokolik, I. N. and Toon, O. B.: Incorporation of mineralogical composition into models of the radiative properties of mineral aerosol from UV to IR wavelengths, *J. Geophys. Res.-Atmos.*, 104, 9423–9444, 1999.
- 950 Steyer, T. R.: Infrared optical properties of some solids of possible interest in astronomy and atmospheric physics, PhD thesis, Dep. of Phys., Univ. of Ariz., Tucson, 1974.
- Todd, M. C., Washington, R., Martins, J. V., Dubovik, O., Lizcano, G., M'Bainayel, S., and Engelstaedter, S.: Mineral dust emission from the Bodélé Depression northern Chad, during BoDEx 2005, *J. Geophys. Res.-Atmos.*, 112, 1–12, <https://doi.org/10.1029/2006JD007170>, 2007.
- 955 Torrent, J., Schwertmann, U., Fechter, H., and Alferez, F.: Quantitative relationships between soil color and hematite content. *Soil Science*, 136, 354–358, 1983.



- Vernon, R. C.: Extinction Coefficient of Single-Crystal Hematite in the Region 3600–7000 Å. *Journal of Applied Physics*, 33, 2140-2141, 1962.
- 960 Viscarra Rossel, R. A., Bui, E. N., De Caritat, P., and McKenzie, N. J.: Mapping iron oxides and the color of Australian soil using visible–near-infrared reflectance spectra. *Journal of Geophysical Research: Earth Surface*, 115, 2010.
- Volz, F. E.: Infrared optical constants of ammonium sulfate, Sahara dust, volcanic pumice, and flyash. *Applied Optics*, 12, 564-568, 1973.
- Walker, A. L., M. Liu, S. D. Miller, K. A. Richardson, and D. L. Westphal: Development of a dust source database for mesoscale forecasting in southwest Asia, *J. Geophys. Res.*, 114, <https://doi.org/10.1029/2008JD011541>, 2009.
- 965 Wang, L., Li, Z., Tian, Q., Ma, Y., Zhang, F., Zhang, Y., Li, D., Li, K., and Li, L.: Estimate of aerosol absorbing components of black carbon, brown carbon, and dust from ground-based remote sensing data of sun-sky radiometers, *J. Geophys. Res.-Atmos.*, 118, 6534–6543, <https://doi.org/10.1002/jgrd.50356>, 2013.
- Yu, Y., Notaro, M., Kalashnikova, O. V., and Garay, M. J.: Climatology of summer Shamal wind in the Middle East. *Journal of Geophysical Research: Atmospheres*, 121, 289-305, <https://doi.org/10.1002/2015JD024063>, 2016.
- 970 Zhang, X. L., Wu, G. J., Zhang, C. L., Xu, T. L., and Zhou, Q. Q.: What is the real role of iron oxides in the optical properties of dust aerosols?, *Atmos. Chem. Phys.*, 15, 12159–12177, <https://doi.org/10.5194/acp-15-12159-2015>, 2015.